

MOJAVE: MONITORING OF JETS IN ACTIVE GALACTIC NUCLEI WITH VLBA EXPERIMENTS. VII. BLAZAR JET ACCELERATION

D. C. HOMAN¹, M. KADLER^{2,3,4,5}, K. I. KELLERMANN⁶, Y. Y. KOVALEV^{7,8}, M. L. LISTER⁹, E. ROS^{7,10}, T. SAVOLAINEN⁷, AND
 J. A. ZENSUS⁷

¹ Department of Physics and Astronomy, Denison University, Granville, OH 43023, USA; homand@denison.edu

² Dr. Remeis-Sternwarte Bamberg, Universität Erlangen-Nürnberg, Sternwartstrasse 7, 96049 Bamberg, Germany

³ Erlangen Centre for Astroparticle Physics, Erwin-Rommel Str. 1, 91058 Erlangen, Germany

⁴ CRESST/NASA Goddard Space Flight Center, Greenbelt, MD 20771, USA

⁵ Universities Space Research Association, 10211 Wincopin Circle, Suite 500 Columbia, MD 21044, USA; matthias.kadler@sternwarte.uni-erlangen.de

⁶ National Radio Astronomy Observatory, 520 Edgemont Road, Charlottesville, VA 22903-2475, USA; kkellerm@nrao.edu

⁷ Max-Planck-Institut für Radioastronomie, Auf dem Hügel 69, D-53121 Bonn, Germany; Eduardo.Ros@uv.es, tsavolainen@mpifr-bonn.mpg.de,
zensus@mpifr-bonn.mpg.de

⁸ Astro Space Center of Lebedev Physical Institute, Profsoyuznaya 84/32, 117997 Moscow, Russia; yyk@asc.rssi.ru

⁹ Department of Physics, Purdue University, 525 Northwestern Avenue, West Lafayette, IN 47907, USA; mlister@purdue.edu

¹⁰ Departament d'Astronomia i Astrofísica, Universitat de València, E-46100 Burjassot, València, Spain

Received 2009 September 11; accepted 2009 September 28; published 2009 November 11

ABSTRACT

We discuss acceleration measurements for a large sample of extragalactic radio jets from the Monitoring Of Jets in Active Galactic Nuclei with VLBA Experiments (MOJAVE) program, which studies the parsec-scale jet structure and kinematics of a complete, flux-density-limited sample of active galactic nuclei (AGNs). Accelerations are measured from the apparent motion of individual jet features or “components” which may represent patterns in the jet flow. We find that significant accelerations are common both parallel and perpendicular to the observed component velocities. Parallel accelerations, representing changes in apparent speed, are generally larger than perpendicular acceleration that represent changes in apparent direction. The trend for larger parallel accelerations indicates that a significant fraction of these changes in apparent speed are due to changes in intrinsic speed of the component rather than changes in direction to the line of sight. We find an overall tendency for components with increasing apparent speed to be closer to the base of their jets than components with decreasing apparent speed. This suggests a link between the observed pattern motions and the underlying flow which, in some cases, may increase in speed close to the base and decrease in speed further out; however, common hydrodynamical processes for propagating shocks may also play a role. About half of the components show “non-radial” motion, or a misalignment between the component’s structural position angle and its velocity direction, and these misalignments generally better align the component motion with the downstream emission. Perpendicular accelerations are closely linked with non-radial motion. When observed together, perpendicular accelerations are usually in the correct direction to have caused the observed misalignment.

Key words: BL Lacertae objects: general – galaxies: active – galaxies: jets – quasars: general – radio continuum: galaxies – surveys

1. INTRODUCTION

The acceleration and collimation of powerful extragalactic jets associated with some active galactic nuclei (AGNs) is still not fully understood. While it seems clear that strong magnetic fields associated with the supermassive black hole/accretion disk system play a key role in the initial acceleration and collimation of the jet (e.g., Meier et al. 2001), it is unclear whether this process is largely complete with the conversion of Poynting flux to flow energy on subparsec scales (e.g., Sikora et al. 2005) or continues into the parsec and decaparsec scales observed with very long baseline interferometry (VLBI). If jets are still being accelerated and collimated on these longer length scales, is the process largely hydrodynamic in nature, or is there still a significant, perhaps dominant, magnetic contribution as suggested by Vlahakis & Königl (2004)?

To date, the observational evidence from VLBI observations of blazar jets on parsec to decaparsec scales presents a mixed picture. Detailed studies of individual jets have reported changes in speed and trajectory of particular components (bright jet features) as well as speed differences between multiple components in the same jet (e.g., Wardle et al. 1994; Zensus et al. 1995; Wehrle et al. 2001; Gómez et al. 2001; Homan

et al. 2003; Bach et al. 2005; Savolainen et al. 2006); however, taken together there is no clear trend for how, or if, jets accelerate on parsec-scales. In a larger study of gamma-ray blazars, Jorstad et al. (2005) reported accelerations in nine of the 15 jets they studied, and these tended to be positive accelerations, indicating increased apparent speed, although they could not determine whether the observed accelerations were due to changes in intrinsic speed or direction of the components. Other authors of multi-jet studies have reported a tendency for more distant jet components to have faster speeds than nearby components in the same object (Homan et al. 2001; Piner et al. 2006; Britzen et al. 2008); however, Homan et al. (2001) also looked for accelerations in the motions of individual jet components and did not find evidence for large accelerations. Kellermann et al. (2004) pointed out that higher frequency VLBI studies tend to observe systematically faster speeds than lower frequency studies which probe longer length scales, suggesting that components are instead faster at smaller jet separations.

Large apparent opening angles and variations in jet ejection angles are common in VLBI observations of blazar jets (e.g., Stirling et al. 2003; Jorstad et al. 2004, 2005; Lister 2006); however, jets observed on kiloparsec scales tend to be well focused

with narrow opening angles. The high incidence of “non-radial” or non-ballistic motion observed on VLBI scales (Kellermann et al. 2004; Piner et al. 2007) suggest that jet components can change direction after ejection from the core, and Kellermann et al. (2004) showed that these non-radial motions tend to be in the direction of the downstream flow. Whether these non-radial motions represent evidence for collimation or simply bends in already well collimated jets is unclear; however Homan et al. (2003) did observe a large, sudden ($\simeq 25^\circ$) change in trajectory in a powerful jet component in 3C 279 to better align with the direction and speed of other jet components and the arcsecond jet direction. Given the wide variety of ejection angles and apparent speeds in this jet (e.g., Wehrle et al. 2001), Homan et al. suggested that this event was evidence that the collimation process may continue even to kiloparsec scales (de-projected). Jorstad et al. (2004) observed a similar change in another jet component in this same jet, but much closer to the base of the jet.

Here, we report the results of the first large-scale study of accelerations in the apparent motions of blazar jets. We examine accelerations both parallel and perpendicular to the apparent component velocities, representing changes in apparent speed and direction, respectively, and we analyze these acceleration measurements for 203 of the best-determined jet component motions from the MOJAVE program (Lister & Homan 2005; Lister et al. 2009b.) This work is an extension of our kinematical analysis of the MOJAVE I sample (Lister et al. 2009c, hereafter Paper VI). MOJAVE stands for Monitoring Of Jets in Active Galactic Nuclei with VLBA Experiments, and it is an ongoing program using the National Radio Astronomy Observatory’s Very Long Baseline Array (VLBA) to monitor the parsec-scale structure and polarization of the brightest AGN jets at $\lambda 2$ cm. MOJAVE builds upon the older *2 cm Survey* (Kellermann et al. 1998; Zensus et al. 2002; Kellermann et al. 2004; Kovalev et al. 2005), and thus, in some cases, our time baseline for kinematical study of jet components spans more than a decade. Previous publications from the MOJAVE program have studied the parsec-scale polarization properties of the MOJAVE I sample (Lister & Homan 2005; Homan & Lister 2006), their VLA structure (Cooper et al. 2007), their parent luminosity function (Cara & Lister 2008), and the connection with their gamma-ray properties measured by the *Fermi* satellite (Kovalev et al. 2009; Lister et al. 2009a).

This paper is organized as follows. Section 2 summarizes key relationships describing the connection between observed accelerations and changes in intrinsic properties of the component or pattern motion, such as Lorentz factor and angle to the line of sight. Section 3 describes the sample of jet components studied for acceleration and reports the results of our analysis for trends in the observed accelerations. Section 4 discusses our results and a summary of our conclusions appears in Section 5. The appendix provides additional background for Section 2.

2. RELATIONSHIPS FOR ACCELERATING MOTION

In this section, we summarize relationships describing changes in apparent speed of parsec-scale AGN jet features. These expressions are derived in more detail in the Appendix and build upon the relationships laid out in Blandford & Königl (1979) and sources referenced therein.

A component or pattern moving with an intrinsic speed βc at angle θ to the line of sight will exhibit an observed motion

given by the familiar form

$$\beta_{\text{obs}} = \frac{\beta \sin \theta}{1 - \beta \cos \theta}. \quad (1)$$

In practice, we deduce β_{obs} from the observed angular speed, μ , and redshift, z from

$$\beta_{\text{obs}} = \mu D_A (1 + z), \quad (2)$$

where D_A is the angular size distance to the galaxy.

As illustrated in the Appendix, the intrinsic velocity, $\vec{\beta}$, is actually a vector which can change in speed and/or direction, resulting in apparent changes to β_{obs} in the plane of the sky. We characterize these changes as either *parallel* or *perpendicular* to $\vec{\beta}_{\text{obs}}$ or equivalently the observed angular velocity $\vec{\mu}$.

2.1. Apparent Changes Along Component Motion

Changes along the observed motion, or *parallel* accelerations, are given by the following expression (Appendix A.2):

$$\frac{d\beta_{\parallel \text{obs}}}{dt_{\text{obs}}} = \frac{\dot{\beta} \sin \theta + \beta \dot{\theta} (\cos \theta - \beta)}{(1 - \beta \cos \theta)^3}, \quad (3)$$

where $\dot{\beta}$ and $\dot{\theta}$ are the intrinsic rates of change of the component speed and angle to the line of sight, respectively. A key question in the evaluation of our observational results is the extent to which we can attribute any observed parallel accelerations to changes in the intrinsic component speed, β , and in Section 2.2 we look at the ratio of parallel to perpendicular accelerations as a possible diagnostic.

If observed parallel accelerations are due entirely to changes in the component’s intrinsic speed, β , or equivalently Lorentz factor, $\Gamma = 1/\sqrt{1 - \beta^2}$, we find the simple relation:

$$\frac{\dot{\beta}_{\parallel \text{obs}}}{\beta_{\text{obs}}} = \frac{\dot{\mu}_{\parallel}}{\mu} (1 + z) = \frac{\dot{\Gamma}}{\Gamma} \frac{\delta^2}{\beta^2}, \quad (4)$$

where we have taken the ratio with the apparent speed β_{obs} and substituted the Doppler factor for the component motion: $\delta = 1/(\Gamma(1 - \beta \cos \theta))$. Taking the ratio with apparent speed provides a convenient measure that can be easily compared between jets and constructed directly from the observed angular motion.

Hence, under the assumption that all of the observed parallel acceleration is due to intrinsic speed changes of the component or pattern, the ratio of observed angular acceleration to observed angular speed gives a fairly simple result in terms of intrinsic changes in the component’s Lorentz factor. The δ^2 term implies that small rates of change in intrinsic Lorentz factor should be greatly magnified in the observed angular acceleration for the high δ jets typical of the MOJAVE I sample (e.g., Paper VI).

2.2. Apparent Changes Perpendicular to the Component Motion

“Perpendicular” accelerations, or changes in motion transverse to the apparent motion on the plane of the sky, are given by the following expression (Appendix A.2):

$$\frac{d\beta_{\perp \text{obs}}}{dt_{\text{obs}}} = \frac{\beta \dot{\phi} \sin \theta}{(1 - \beta \cos \theta)^2}, \quad (5)$$

where ϕ is the azimuthal angle of the both the component's intrinsic velocity, $\vec{\beta}$, and its apparent velocity in the plane of the sky, $\vec{\beta}_{\text{obs}}$. See the [Appendix](#) for an explanation of the geometry of $\vec{\beta}$.

The relative magnitudes of observed parallel and perpendicular accelerations may give us information about how much of any observed parallel acceleration is due to intrinsic changes in component speed as opposed to changes in its angle to the line of sight. If all the apparent acceleration is due only to changes in direction of the component motion, we can divide Equation (3) by Equation (5) and set $\dot{\beta} = 0$ to get the following expression:

$$\frac{d\beta_{\parallel\text{obs}}/dt_{\text{obs}}}{d\beta_{\perp\text{obs}}/dt_{\text{obs}}} = \frac{\dot{\beta}_{\theta} \cos \theta - \beta}{\dot{\beta}_{\phi} (1 - \beta \cos \theta)} = \frac{\dot{\beta}_{\theta}}{\dot{\beta}_{\phi}} \cos \theta_{ab}. \quad (6)$$

Here, θ_{ab} is the aberrated angle to the line of sight in the frame comoving with the jet component and we have defined $\dot{\beta}_{\theta} = \beta \dot{\theta}$ and $\dot{\beta}_{\phi} = \beta \dot{\phi} \sin \theta$. By symmetry, we expect that $\dot{\beta}_{\theta}$ and $\dot{\beta}_{\phi}$, the components of directional change of $\vec{\beta}$, will be of similar magnitude when averaged over many jets. For components moving at the critical angle for maximal superluminal motion, $\cos \theta = \beta$, $\cos \theta_{ab} = 0$, and small changes in θ will not change the apparent speed, β_{obs} ; thus only perpendicular acceleration is possible from a change in direction. A typical beamed jet in a flux-density-limited survey like MOJAVE has an angle to the line of sight $\theta \sim 0.5\Gamma^{-1}$ (Lister & Marscher 1997) giving $\cos \theta_{ab} \simeq 0.6$. Therefore, if all of the observed accelerations in our sample are due to changes in direction rather than intrinsic changes in speed or Lorentz factor, we expect the observed parallel accelerations to be about 60% of the magnitude of perpendicular accelerations when averaged across our sample.

3. DATA AND RESULTS

In Paper VI, we reported proper motion results for the MOJAVE I complete sample of 135 parsec-scale radio jets. Vector proper motions were fit to position versus time data for 526 robust components in 127 of the 135 jets. In each jet, component positions were measured relative to the jet base or “core” which was assumed to be stationary from epoch to epoch. For the 311 components with 10 or more epochs of observation, constant acceleration terms were included in the apparent proper motion fit, resulting in measurement of the apparent parallel, $\dot{\mu}_{\parallel}$, and perpendicular, $\dot{\mu}_{\perp}$, acceleration. These parallel and perpendicular directions are taken relative to the average vector proper motion on the sky and thus represent changes in apparent speed and direction, respectively. As described in Paper VI, these accelerations are measured relative to the middle epoch, and they represent constant apparent acceleration applied only during the observed epochs. We do not know if the same or different accelerations were applied to the component motion prior to our observations. Procedural details and full results of the proper motion fitting are presented in Paper VI, and here we discuss a subset of components with the highest quality proper motion measurements to investigate the properties of non-radial and accelerated motion observed in our sample.

For this analysis, we restrict our sample of jet motions to those having a proper motion, μ , of at least 3σ significance, ≥ 10 epochs (required for our acceleration analysis), a known redshift (required for relative acceleration analysis of $\dot{\beta}_{\text{obs}}/\beta_{\text{obs}}$), and an uncertainty in misalignment angle, $|\langle\vartheta\rangle - \phi|$, of no more than 5° between the average component position angle, $\langle\vartheta\rangle$, and vector proper motion position angle, ϕ . This limit guarantees that both

angles in this quantity are well determined, and therefore that the meaning of the parallel and perpendicular accelerations, defined relative to ϕ , are unambiguous. A total of 203 jet components meet these criteria, and these components are listed in Table 1 along with selected properties from the proper motion results.

Plots illustrating examples of accelerated motion in a few of the components in our sample are briefly discussed in the following subsection. Separation versus time and sky position plots for all the 203 jet components analyzed in this paper, along with the entire MOJAVE sample, are included in Paper VI. In the remainder of this section, we present results on the general properties of non-radial motions and accelerations, and we specifically investigate a number of key relationships including: (1) the connection between non-radial motion and downstream jet structure, (2) the relative magnitudes of apparent parallel and perpendicular accelerations which are either along or transverse to the component motion respectively, (3) the magnitude and sign of accelerations as a function of distance along the jet, and (4) the relationship between observed accelerations and non-radial motion.

3.1. Examples of Accelerated Motion

Figures 1 and 2 illustrate examples of the types of motion observed in the components in our sample. Six components are illustrated, three per figure. Each row of the figures shows the motion of one component in three ways: first superimposed on the jet structure at a middle epoch of our observations, second as a zoomed-in view to better show the motion on the sky, and third as a radial distance versus time plot to illustrate the speed of the component as a function of time. Each panel also contains a colored solid line indicating our best fit to the component position versus time including acceleration terms.

The first two rows of Figure 1 show components 6 and 7 of 0333+321. Component 6 is an example of a component which is moving radially outward at a constant speed and doesn't show signs of acceleration. Component 7 is further out in the jet and is moving non-radially in the direction of the downstream flow. Component 7 is also showing a significant negative parallel acceleration, i.e., it is slowing down during our observations. While the trajectory of component 7 in the middle panel appears somewhat curved, the measured perpendicular acceleration is not significant.

The last row of Figure 1 shows the motion of component 3 from 1222+216. The trajectory is clearly curved to the east as the component follows the bent path of the jet, and the measured perpendicular acceleration corresponding to this curvature is highly significant. There is no accompanying change in the apparent speed of the component as indicated by the lack of significant parallel acceleration. It is interesting that four jet components in 1222+216 show essentially the same motion with significant perpendicular accelerations producing curving motion to the east, indicating a stable curved path for the jet out to about 10 mas from the jet core. It is interesting that this “stable” path is not directed toward the most distant jet component, component 1, which seems to be following its own, roughly parallel trajectory, at about half the apparent speed of the other features.

Some jets, like 1222+216, show consistent patterns of accelerated motion for several components, while others, like 3C 273 (1226+023), show a wide variety of accelerated or non-radial motion types. The first row of Figure 2 shows the motion of component 9 of 3C 273. Component 9 is an example of a component with radially outward motion that is increasing in

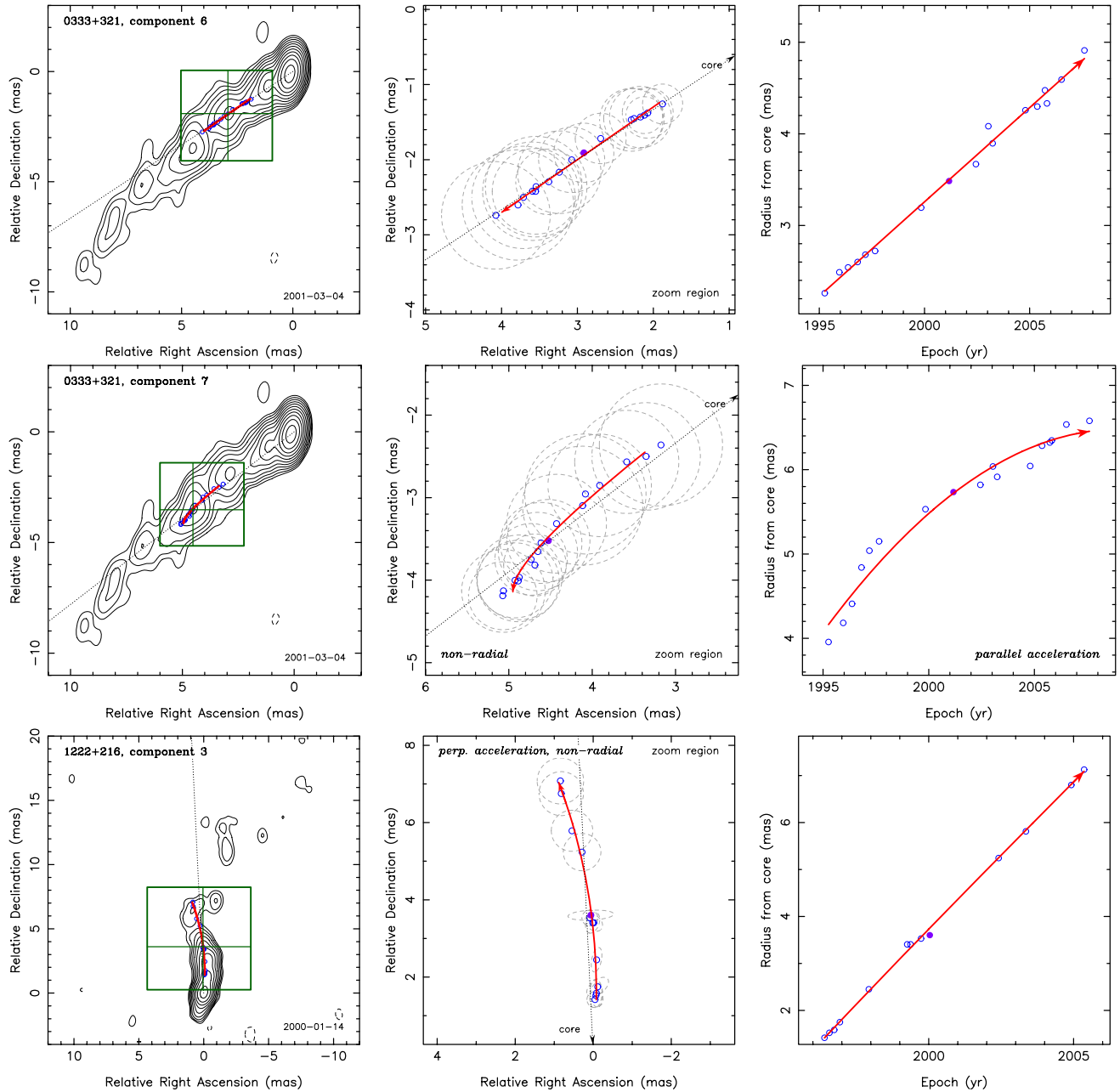


Figure 1. Plots of component trajectories in 0333+321 and 1222+216. One component appears per row. Left-hand panels contain a contour image of the jet for an epoch near the midpoint of the observations of the component. Superimposed on the contour are the sky position of the component for all epochs, a radial line from the jet core to the mean component position, and a projection of our best fit trajectory for the component. Middle panels show a zoomed view of the component's sky positions, radial line, and fitted trajectory. The dotted outlines represent the full width at half-maximum size of the component in each epoch. Right-hand panels show the radial distance of the component from the jet core as a function of time with a projection of our best-fit trajectory.

apparent speed, i.e., it is showing a significant positive parallel acceleration. The component also has a significant perpendicular acceleration, tending to curve the trajectory upward slightly, but this perpendicular acceleration is much smaller than the parallel acceleration producing the observed increase in apparent speed.

Another jet which shows a wide variety of accelerated and non-radial motion types is 1928+738. The component illustrated in the second row of Figure 2, component 3, is an example of a jet component that shows more jitter than is typical in its centroid position from epoch to epoch; however, despite this limitation, our large number of epochs still allow us to determine its mean trajectory very well. We find the component to be moving non-radially toward the downstream jet structure, and we find no

significant acceleration either parallel or perpendicular to the component motion.

Finally, the last row in Figure 2 shows the motion of component 4 in 2223+052. This component is an example of non-radial motion with significant acceleration both parallel to the component velocity, resulting in an increasing apparent speed, and perpendicular to the component velocity, resulting in a trajectory curving toward the downstream jet structure.

3.2. Non-radial Motion

We characterize the extent to which a jet component's motion is non-radial by its misalignment angle, $|\langle\vartheta\rangle - \phi|$. Figure 3 is a histogram of these values for the 203 jet components in our sample. Approximately, one-half of the components ($N = 100$)

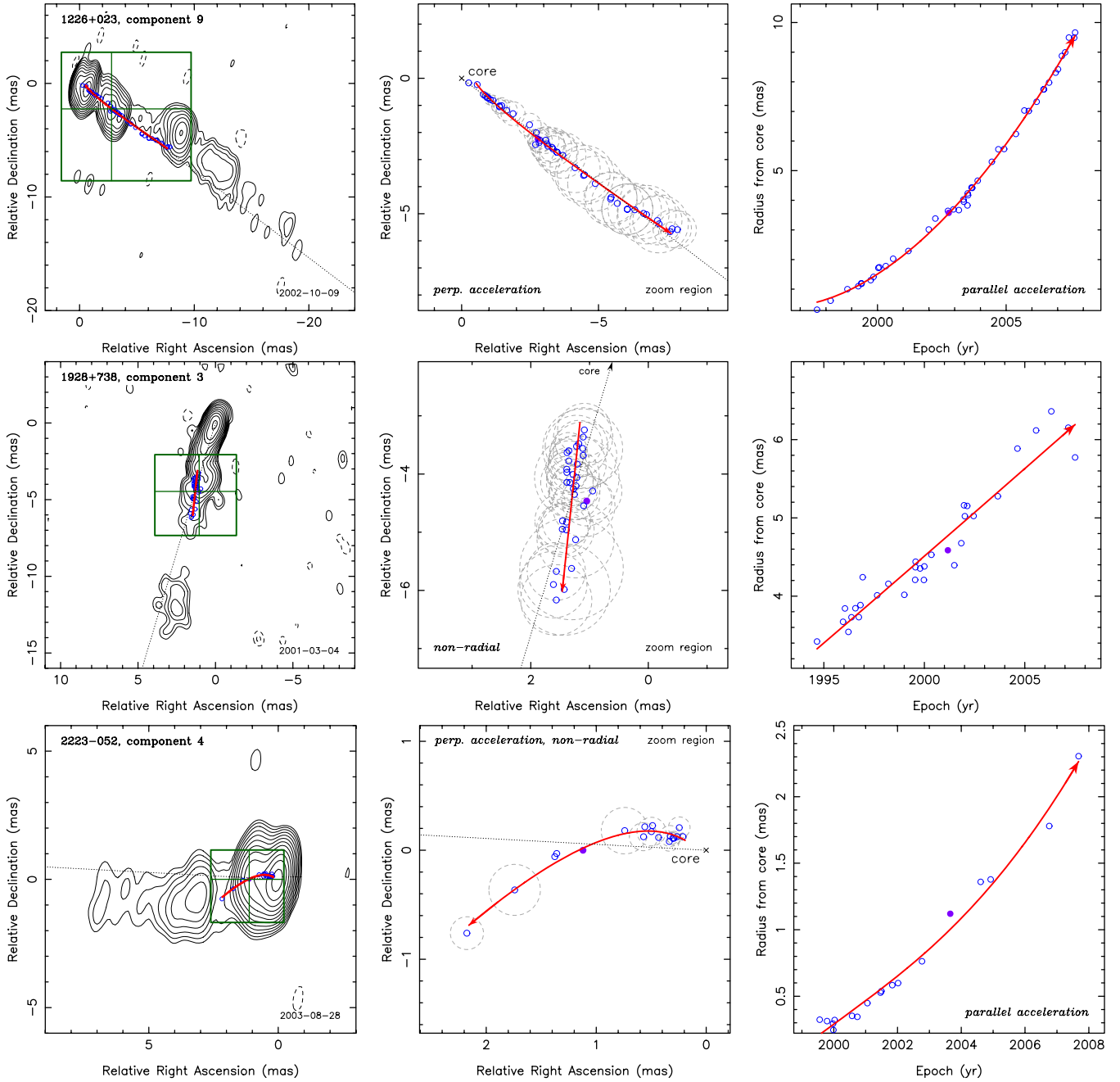


Figure 2. Plots of component trajectories in 3C 273, 1928+738, and 2223-052, otherwise as described for Figure 1.

are significantly non-radial with $|\langle\vartheta\rangle - \phi| > 0$ at the $\geq 3\sigma$ level, and about a fifth ($N = 41$) have large non-radial motion with $|\langle\vartheta\rangle - \phi| \gtrsim 10^\circ$ by at least 2σ .

For each of the significantly non-radial components, we compared the direction of non-radial motion to a contour image of the jet from an epoch close to the middle epoch of that component's trajectory. We found that the large majority of non-radial components, 69 of the 83 for which we could make a determination, are moving in a direction, relative to their radial position angle, which will tend to make them better aligned with the downstream emission. In cases, where the downstream position angle was ambiguous due to a curving jet, we took the next structure in the jet to define the downstream direction. In a few cases, such as 3C 279 component 1, we were able to use the direction of the extended structure from lower-resolution observations to make this comparison.

3.3. Acceleration

Of the 203 jet components in our sample, approximately one-third ($N = 64$) have significant parallel acceleration and one fifth ($N = 44$) have significant perpendicular acceleration with $\dot{\mu}_{\parallel}$ or $\dot{\mu}_{\perp}$ respectively differing from zero at the $\geq 3\sigma$ level.

To compare accelerations in jet components with different apparent speeds, we define relative accelerations as follows:

$$\dot{\eta}_{\parallel} = \dot{\beta}_{\parallel\text{obs}}/\beta_{\text{obs}} = (1+z)\dot{\mu}_{\parallel}/\mu \quad (7)$$

and

$$\dot{\eta}_{\perp} = \dot{\beta}_{\perp\text{obs}}/\beta_{\text{obs}} = (1+z)\dot{\mu}_{\perp}/\mu. \quad (8)$$

These relative accelerations are computed for each component in our sample, and they are listed in Table 1. We define components with “high” acceleration as those with relative accelerations

Table 1
Components for Acceleration and Non-radial Motion Analysis

Source	I.D.	N	$\langle R \rangle$ (mas)	$\langle \vartheta \rangle$ (deg.)	d_{proj} (pc)	μ ($\mu\text{as yr}^{-1}$)	β_{obs}	ϕ (deg.)	$ \langle \vartheta \rangle - \phi $ (deg.)	$\dot{\mu}_{\parallel}$ ($\mu\text{as yr}^{-2}$)	$\dot{\mu}_{\perp}$ ($\mu\text{as yr}^{-2}$)	$\dot{\eta}_{\parallel}$	$\dot{\eta}_{\perp}$
(1)	(2)	(3)	(4)	(5)	(6)	(7)	(8)	(9)	(10)	(11)	(12)	(13)	(14)
0016+731	1	12	1.10	137.3	9.40	87 ± 5	6.7 ± 0.4	152.1 ± 2.6	14.7 ± 2.8	4 ± 3	5 ± 2	0.14 ± 0.09	0.16 ± 0.07
0059+581	2	13	1.46	-119.2	10.07	197 ± 14	7.3 ± 0.5	-106.7 ± 4.3	12.5 ± 4.5	49 ± 13	-2 ± 15	0.41 ± 0.11	-0.01 ± 0.12
	3	10	0.81	-125.8	5.58	283 ± 20	10.5 ± 0.7	-111.3 ± 3.8	14.5 ± 4.0	-20 ± 45	-14 ± 43	-0.11 ± 0.26	-0.08 ± 0.25
	4	10	0.59	-163.8	4.07	162 ± 13	6.0 ± 0.5	-129.3 ± 4.8	34.4 ± 5.0	-35 ± 29	10 ± 30	-0.36 ± 0.29	0.10 ± 0.31
0202+319	1	10	7.42	-5.9	63.30	121 ± 11	8.2 ± 0.8	-38.7 ± 5.0	32.8 ± 5.0	8 ± 10	-9 ± 10	0.16 ± 0.21	-0.18 ± 0.20
0212+735	1	14	0.84	115.8	6.95	84 ± 3	7.5 ± 0.3	102.0 ± 1.8	13.7 ± 1.9	-6 ± 2	-5 ± 1	-0.23 ± 0.06	-0.22 ± 0.06
0215+015	2	12	2.12	107.2	18.14	451 ± 28	33.8 ± 2.1	104.5 ± 2.2	2.7 ± 2.4	-47 ± 36	11 ± 24	-0.28 ± 0.21	0.06 ± 0.14
0234+285	3	15	3.89	-11.8	32.50	199 ± 11	11.9 ± 0.7	4.7 ± 1.1	16.4 ± 1.1	-3 ± 8	-10 ± 3	-0.04 ± 0.09	-0.11 ± 0.03
0238-084	3	24	9.46	68.8	0.98	594 ± 23	0.2 ± 0.0	67.1 ± 2.0	1.7 ± 2.1	-47 ± 16	8 ± 16	-0.08 ± 0.03	0.01 ± 0.03
(NGC 1052)	4	14	6.80	72.3	0.71	873 ± 37	0.3 ± 0.0	74.7 ± 2.2	2.3 ± 2.2	105 ± 47	38 ± 51	0.12 ± 0.05	0.04 ± 0.06
	5	12	5.38	69.6	0.56	746 ± 48	0.3 ± 0.0	69.9 ± 2.0	0.3 ± 2.0	170 ± 67	-11 ± 36	0.23 ± 0.09	-0.02 ± 0.05
	10	10	2.35	68.6	0.24	986 ± 50	0.3 ± 0.0	72.2 ± 1.4	3.7 ± 1.5	185 ± 178	300 ± 85	0.19 ± 0.18	0.31 ± 0.09
	11	13	2.71	67.7	0.28	804 ± 34	0.3 ± 0.0	71.0 ± 1.4	3.3 ± 1.5	-102 ± 48	36 ± 22	-0.13 ± 0.06	0.04 ± 0.03
	12	12	2.40	66.5	0.25	696 ± 26	0.2 ± 0.0	67.9 ± 1.6	1.3 ± 1.6	-219 ± 50	-33 ± 36	-0.32 ± 0.07	-0.05 ± 0.05
	14	10	1.57	66.2	0.16	595 ± 36	0.2 ± 0.0	67.3 ± 1.7	1.2 ± 1.9	25 ± 99	2 ± 48	0.04 ± 0.17	0.00 ± 0.08
	17	10	3.65	68.3	0.38	1033 ± 31	0.4 ± 0.0	71.3 ± 1.4	3.0 ± 1.5	-114 ± 61	32 ± 52	-0.11 ± 0.06	0.03 ± 0.05
	26	10	2.68	-114.7	0.28	751 ± 56	0.3 ± 0.0	-111.7 ± 2.8	3.0 ± 3.0	154 ± 110	82 ± 79	0.21 ± 0.15	0.11 ± 0.11
	30	13	2.15	-111.4	0.22	807 ± 42	0.3 ± 0.0	-115.2 ± 1.7	3.8 ± 1.9	185 ± 60	-26 ± 34	0.23 ± 0.08	-0.03 ± 0.04
	31	10	2.47	-114.6	0.26	819 ± 57	0.3 ± 0.0	-121.1 ± 3.3	6.5 ± 3.5	199 ± 95	19 ± 82	0.24 ± 0.12	0.02 ± 0.10
	33	21	6.51	-111.9	0.68	773 ± 24	0.3 ± 0.0	-112.6 ± 1.7	0.7 ± 1.8	-77 ± 16	5 ± 15	-0.10 ± 0.02	0.01 ± 0.02
	34	13	6.66	-112.8	0.69	1012 ± 46	0.3 ± 0.0	-117.5 ± 2.8	4.7 ± 2.9	15 ± 75	-152 ± 75	0.01 ± 0.07	-0.15 ± 0.08
	35	18	14.65	-114.7	1.52	751 ± 42	0.3 ± 0.0	-109.4 ± 3.7	5.3 ± 3.7	16 ± 27	55 ± 30	0.02 ± 0.04	0.07 ± 0.04
0316+413 (3C 84)	1	22	13.74	178.3	4.87	266 ± 50	0.3 ± 0.1	173.2 ± 3.0	5.1 ± 3.1	102 ± 38	-10 ± 11	0.39 ± 0.16	-0.04 ± 0.04
0333+321	6	17	3.56	123.7	29.93	206 ± 3	12.7 ± 0.2	125.0 ± 0.9	1.4 ± 1.0	2 ± 2	3 ± 2	0.02 ± 0.03	0.03 ± 0.03
(NRAO 140)	7	17	5.57	127.9	46.82	188 ± 7	11.6 ± 0.4	136.9 ± 2.3	8.9 ± 2.3	-24 ± 5	8 ± 5	-0.28 ± 0.06	0.09 ± 0.06
0336-019	4	10	1.39	49.9	10.68	253 ± 16	11.7 ± 0.7	56.9 ± 4.0	7.0 ± 4.4	8 ± 17	-11 ± 19	0.06 ± 0.13	-0.08 ± 0.14
0415+379	7	12	9.59	64.7	9.10	1677 ± 41	5.5 ± 0.1	64.5 ± 1.0	0.2 ± 1.1	101 ± 42	2 ± 31	0.06 ± 0.03	0.00 ± 0.02
(3C 111)	9	11	7.29	65.5	6.91	1269 ± 31	4.2 ± 0.1	66.3 ± 1.3	0.8 ± 1.4	167 ± 38	41 ± 35	0.14 ± 0.03	0.03 ± 0.03
0430+052	1	14	9.74	-108.0	6.35	2187 ± 93	4.9 ± 0.2	-101.8 ± 1.4	6.2 ± 1.4	1705 ± 547	11 ± 323	0.81 ± 0.26	0.01 ± 0.15
(3C 120)	2	22	6.38	-106.8	4.16	1730 ± 21	3.9 ± 0.1	-102.1 ± 0.7	4.7 ± 0.8	-43 ± 33	142 ± 35	-0.03 ± 0.02	0.08 ± 0.02
	3	15	7.20	-116.1	4.69	2307 ± 27	5.1 ± 0.1	-113.2 ± 0.9	2.9 ± 0.9	202 ± 86	27 ± 133	0.09 ± 0.04	0.01 ± 0.06
	4	13	5.03	-116.5	3.28	1940 ± 91	4.3 ± 0.2	-108.9 ± 1.2	7.5 ± 1.2	1309 ± 458	267 ± 221	0.70 ± 0.25	0.14 ± 0.12
	5	15	3.93	-123.8	2.56	1772 ± 45	3.9 ± 0.1	-115.5 ± 1.4	8.2 ± 1.4	601 ± 160	50 ± 153	0.35 ± 0.09	0.03 ± 0.09
	6	15	3.14	-122.7	2.05	1939 ± 70	4.3 ± 0.2	-119.8 ± 2.2	2.9 ± 2.3	-186 ± 257	168 ± 267	-0.10 ± 0.14	0.09 ± 0.14
	7	14	2.11	-120.0	1.37	2091 ± 38	4.7 ± 0.1	-122.0 ± 1.0	2.0 ± 1.0	202 ± 222	247 ± 218	0.10 ± 0.11	0.12 ± 0.11
	8	13	0.97	-119.8	0.63	1506 ± 46	3.4 ± 0.1	-114.8 ± 1.2	5.0 ± 1.3	-234 ± 302	145 ± 191	-0.16 ± 0.21	0.10 ± 0.13
	11	11	8.73	-117.0	5.69	2109 ± 31	4.7 ± 0.1	-116.8 ± 0.7	0.3 ± 0.7	349 ± 62	28 ± 50	0.17 ± 0.03	0.01 ± 0.02
	12	12	7.08	-116.7	4.61	2224 ± 70	5.0 ± 0.2	-116.0 ± 1.5	0.7 ± 1.7	255 ± 107	-3 ± 96	0.12 ± 0.05	-0.00 ± 0.04
	24	11	2.90	-111.2	1.89	1906 ± 40	4.2 ± 0.1	-105.7 ± 0.7	5.5 ± 0.7	-179 ± 156	-17 ± 96	-0.10 ± 0.08	-0.01 ± 0.05
0458-020	2	10	4.64	-55.6	38.65	185 ± 9	16.3 ± 0.8	-55.8 ± 2.9	0.2 ± 2.9	-36 ± 6	3 ± 6	-0.65 ± 0.11	0.05 ± 0.11
	3	10	2.19	-45.5	18.24	152 ± 9	13.4 ± 0.8	-58.2 ± 3.2	12.8 ± 3.3	-5 ± 6	2 ± 6	-0.11 ± 0.13	0.03 ± 0.12
0528+134	2	18	1.90	35.4	16.05	227 ± 5	18.9 ± 0.4	21.6 ± 1.0	13.8 ± 1.1	18 ± 4	-4 ± 3	0.25 ± 0.05	-0.05 ± 0.04
	3	22	1.16	42.2	9.80	142 ± 10	11.8 ± 0.8	27.6 ± 3.0	14.6 ± 3.4	-19 ± 6	-1 ± 5	-0.42 ± 0.14	-0.03 ± 0.10
0605-085	2	14	4.74	113.4	36.68	254 ± 23	12.0 ± 1.1	118.8 ± 3.3	5.4 ± 3.3	17 ± 14	-6 ± 9	0.13 ± 0.10	-0.04 ± 0.07
	3	15	2.78	122.5	21.51	419 ± 13	19.8 ± 0.6	122.2 ± 1.3	0.3 ± 1.5	28 ± 7	-2 ± 5	0.12 ± 0.03	-0.01 ± 0.02
	4	12	1.42	123.4	10.99	355 ± 9	16.7 ± 0.4	123.3 ± 1.2	0.2 ± 1.4	8 ± 11	-6 ± 9	0.04 ± 0.06	-0.03 ± 0.05
0716+714	5	10	0.97	18.9	4.39	521 ± 18	10.1 ± 0.3	16.5 ± 1.3	2.4 ± 1.6	194 ± 42	-76 ± 28	0.49 ± 0.11	-0.19 ± 0.07
0736+017	1	12	11.16	-84.7	35.18	358 ± 9	4.4 ± 0.1	-58.2 ± 2.0	26.4 ± 2.0	-41 ± 7	69 ± 9	-0.14 ± 0.02	0.23 ± 0.03
	5	11	5.06	-73.4	15.95	1180 ± 77	14.6 ± 0.9	-77.8 ± 1.8	4.4 ± 2.1	71 ± 69	-49 ± 33	0.07 ± 0.07	-0.05 ± 0.03
0738+313	2	16	4.83	155.2	33.00	246 ± 10	8.9 ± 0.4	126.1 ± 2.4	29.1 ± 2.5	-18 ± 5	7 ± 6	-0.12 ± 0.04	0.05 ± 0.04
	3	17	3.88	161.9	26.51	169 ± 5	6.2 ± 0.2	115.8 ± 1.2	46.0 ± 1.3	1 ± 3	-5 ± 2	0.01 ± 0.02	-0.05 ± 0.02
	6	17	3.34	178.2	22.82	96 ± 3	3.5 ± 0.1	156.9 ± 1.4	21.3 ± 1.4	-5 ± 2	-6 ± 1	-0.08 ± 0.03	-0.11 ± 0.02
	8	14	1.30	-175.5	8.88	153 ± 6	5.6 ± 0.2	-174.8 ± 0.9	0.7 ± 1.0	-1 ± 4	-2 ± 2	-0.01 ± 0.05	-0.02 ± 0.02
0748+126	2	11	3.93	117.4	30.59	383 ± 17	18.3 ± 0.8	120.7 ± 2.6	3.3 ± 2.7	-13 ± 17	-19 ± 16	-0.06 ± 0.08	-0.09 ± 0.08
	3	11	2.38	113.2	18.53	216 ± 13	10.3 ± 0.6	107.9 ± 2.7	5.3 ± 2.8	-19 ± 10	20 ± 9	-0.17 ± 0.09	0.17 ± 0.08
0814+425	2	15	1.42	88.7	5.42	53 ± 3	0.8 ± 0.1	90.0 ± 2.6	1.3 ± 2.6	-6 ± 2	8 ± 2	-0.13 ± 0.05	0.20 ± 0.04
0823+033	7	11	1.65	28.2	10.10	592 ± 27	17.9 ± 0.8	27.3 ± 2.1	0.9 ± 2.4	13 ± 39	-49 ± 30	0.03 ± 0.10	-0.13 ± 0.08
0827+243	2	19	1.97	120.9	15.59	407 ± 13	20.3 ± 0.7	140.9 ± 1.6	20.0 ± 1.7	7 ± 16	51 ± 15	0.03 ± 0.08	0.24 ± 0.07
	3	13	0.88	112.8	6.96	394 ± 25	19.7 ± 1.2	115.5 ± 4.0	2.7 ± 4.5	51 ± 36	36 ± 38	0.25 ± 0.18	0.18 ± 0.19
0829+046	5	15											

Table 1
(Continued)

Source	I.D.	N	$\langle R \rangle$ (mas)	$\langle \vartheta \rangle$ (deg.)	d_{proj} (pc)	μ ($\mu\text{as yr}^{-1}$)	β_{obs}	ϕ (deg.)	$ \langle \vartheta \rangle - \phi $ (deg.)	$\dot{\mu}_{\parallel}$ ($\mu\text{as yr}^{-2}$)	$\dot{\mu}_{\perp}$ ($\mu\text{as yr}^{-2}$)	$\dot{\eta}_{\parallel}$	$\dot{\eta}_{\perp}$
(1)	(2)	(3)	(4)	(5)	(6)	(7)	(8)	(9)	(10)	(11)	(12)	(13)	(14)
0836+710	1	13	12.97	-149.6	108.54	222 \pm 18	19.2 \pm 1.6	-159.2 \pm 2.2	9.6 \pm 2.2	-18 \pm 13	2 \pm 6	-0.26 \pm 0.19	0.03 \pm 0.09
	2	11	8.45	-142.6	70.71	256 \pm 26	22.2 \pm 2.2	-150.1 \pm 4.7	7.6 \pm 4.7	-23 \pm 19	36 \pm 16	-0.29 \pm 0.24	0.46 \pm 0.20
	3	12	3.44	-145.8	28.79	156 \pm 9	13.5 \pm 0.8	-151.5 \pm 2.6	5.8 \pm 2.6	-8 \pm 7	2 \pm 6	-0.16 \pm 0.15	0.04 \pm 0.12
	4	12	2.33	-142.9	19.50	192 \pm 7	16.6 \pm 0.6	-150.3 \pm 1.8	7.4 \pm 1.9	-5 \pm 6	-0 \pm 5	-0.08 \pm 0.10	-0.00 \pm 0.08
	5	12	1.41	-138.8	11.80	224 \pm 8	19.4 \pm 0.7	-146.0 \pm 2.4	7.2 \pm 2.5	-1 \pm 6	-18 \pm 7	-0.01 \pm 0.09	-0.26 \pm 0.10
	6	12	0.77	-139.6	6.44	203 \pm 5	17.6 \pm 0.4	-138.2 \pm 1.5	1.4 \pm 1.8	35 \pm 5	-6 \pm 5	0.56 \pm 0.08	-0.09 \pm 0.07
0838+133	2	14	3.10	79.2	21.90	250 \pm 9	9.7 \pm 0.3	94.3 \pm 2.4	15.1 \pm 2.4	-8 \pm 9	30 \pm 10	-0.05 \pm 0.06	0.20 \pm 0.07
(3C 207)	3	12	2.14	74.6	15.12	334 \pm 30	12.9 \pm 1.2	69.9 \pm 4.6	4.7 \pm 4.6	-96 \pm 101	-233 \pm 82	-0.48 \pm 0.51	-1.17 \pm 0.43
	6	13	0.55	82.9	3.89	54 \pm 7	2.1 \pm 0.3	62.7 \pm 4.7	20.2 \pm 4.7	-17 \pm 27	-32 \pm 16	-0.52 \pm 0.83	-0.99 \pm 0.51
0851+202	1	13	1.00	-93.7	4.48	613 \pm 26	11.8 \pm 0.5	-93.5 \pm 0.7	0.2 \pm 0.8	-222 \pm 64	-55 \pm 18	-0.47 \pm 0.14	-0.12 \pm 0.04
(OJ287)	4	10	1.48	-116.2	6.64	795 \pm 20	15.3 \pm 0.4	-104.9 \pm 2.3	11.3 \pm 2.4	60 \pm 120	65 \pm 190	0.10 \pm 0.20	0.11 \pm 0.31
	5	19	1.18	-115.9	5.29	540 \pm 6	10.4 \pm 0.1	-102.7 \pm 0.4	13.2 \pm 0.4	-132 \pm 22	125 \pm 13	-0.32 \pm 0.05	0.30 \pm 0.03
	9	13	1.12	-121.3	5.02	462 \pm 38	8.9 \pm 0.7	-110.5 \pm 3.1	10.8 \pm 3.2	-245 \pm 84	46 \pm 55	-0.69 \pm 0.24	0.13 \pm 0.16
	15	24	3.35	-109.3	15.02	273 \pm 21	5.2 \pm 0.4	-111.1 \pm 4.5	1.8 \pm 4.5	-9 \pm 32	33 \pm 32	-0.05 \pm 0.15	0.16 \pm 0.15
0917+624	3	12	2.66	-13.1	22.67	229 \pm 17	15.4 \pm 1.1	-13.0 \pm 3.0	0.1 \pm 3.1	-74 \pm 19	-26 \pm 13	-0.79 \pm 0.21	-0.28 \pm 0.14
	4	10	1.41	-22.0	12.02	179 \pm 24	12.1 \pm 1.6	-8.8 \pm 4.7	13.2 \pm 4.8	-21 \pm 36	-31 \pm 20	-0.28 \pm 0.49	-0.42 \pm 0.28
	5	11	0.89	-31.7	7.59	135 \pm 8	9.1 \pm 0.5	-15.3 \pm 2.8	16.4 \pm 2.9	-5 \pm 10	-36 \pm 8	-0.08 \pm 0.18	-0.66 \pm 0.15
0945+408	1	12	11.55	113.4	96.98	200 \pm 18	12.2 \pm 1.1	113.3 \pm 4.8	0.1 \pm 4.9	-15 \pm 9	7 \pm 10	-0.17 \pm 0.10	0.08 \pm 0.11
	4	11	1.23	114.0	10.33	217 \pm 11	13.3 \pm 0.7	114.6 \pm 1.7	0.6 \pm 1.9	16 \pm 7	-5 \pm 4	0.17 \pm 0.07	-0.05 \pm 0.05
1055+018	3	23	3.91	-49.8	30.45	229 \pm 21	11.0 \pm 1.0	-87.3 \pm 4.8	37.5 \pm 4.9	-13 \pm 20	23 \pm 18	-0.11 \pm 0.16	0.19 \pm 0.15
1127-145	4	13	4.16	80.9	34.65	239 \pm 10	14.1 \pm 0.6	84.0 \pm 1.9	3.1 \pm 2.0	6 \pm 7	8 \pm 5	0.05 \pm 0.06	0.07 \pm 0.05
1150+812	2	10	3.02	170.2	25.36	105 \pm 5	6.4 \pm 0.3	155.3 \pm 3.7	15.0 \pm 3.7	-1 \pm 4	-1 \pm 6	-0.03 \pm 0.08	-0.03 \pm 0.12
	3	10	2.62	179.8	22.00	115 \pm 5	7.0 \pm 0.3	172.0 \pm 3.2	7.9 \pm 3.2	-5 \pm 4	-11 \pm 4	-0.10 \pm 0.08	-0.21 \pm 0.08
	4	10	1.40	-160.6	11.76	111 \pm 5	6.8 \pm 0.3	-171.3 \pm 1.3	10.7 \pm 1.3	9 \pm 4	-19 \pm 2	0.19 \pm 0.08	-0.38 \pm 0.04
1156+295	4	10	0.71	-3.3	5.16	327 \pm 27	13.4 \pm 1.1	6.9 \pm 1.1	10.2 \pm 1.2	55 \pm 59	-132 \pm 14	0.29 \pm 0.31	-0.70 \pm 0.09
1222+216	1	16	12.43	-7.8	69.59	339 \pm 13	8.9 \pm 0.3	7.7 \pm 3.0	15.6 \pm 3.0	-4 \pm 10	17 \pm 13	-0.02 \pm 0.04	0.07 \pm 0.06
	2	16	7.15	6.6	40.03	575 \pm 16	15.1 \pm 0.4	12.7 \pm 1.4	6.1 \pm 1.4	-13 \pm 12	36 \pm 10	-0.03 \pm 0.03	0.09 \pm 0.03
	3	13	3.66	2.7	20.49	636 \pm 7	16.7 \pm 0.2	9.7 \pm 0.3	7.0 \pm 0.4	-2 \pm 6	26 \pm 3	-0.00 \pm 0.01	0.06 \pm 0.01
	4	16	3.25	-0.9	18.20	633 \pm 7	16.6 \pm 0.2	5.0 \pm 0.5	5.9 \pm 0.6	8 \pm 5	32 \pm 4	0.02 \pm 0.01	0.07 \pm 0.01
	5	11	3.24	-5.9	18.14	643 \pm 13	16.9 \pm 0.3	0.0 \pm 0.4	5.9 \pm 0.5	-27 \pm 14	27 \pm 5	-0.06 \pm 0.03	0.06 \pm 0.01
1226+023	1	14	18.69	-123.7	50.50	820 \pm 53	8.5 \pm 0.6	-143.5 \pm 3.4	19.8 \pm 3.4	215 \pm 112	66 \pm 100	0.30 \pm 0.16	0.09 \pm 0.14
(3C 273)	2	50	13.63	-122.1	36.83	727 \pm 10	7.5 \pm 0.1	-128.5 \pm 0.8	6.4 \pm 0.8	52 \pm 6	-34 \pm 6	0.08 \pm 0.01	-0.05 \pm 0.01
	3	19	6.33	-113.3	17.10	1046 \pm 17	10.8 \pm 0.2	-117.8 \pm 0.9	4.5 \pm 1.0	-78 \pm 33	-8 \pm 36	-0.09 \pm 0.04	-0.01 \pm 0.04
	5	53	8.69	-117.8	23.48	1099 \pm 7	11.3 \pm 0.1	-118.9 \pm 0.3	1.1 \pm 0.3	-77 \pm 4	-36 \pm 4	-0.08 \pm 0.00	-0.04 \pm 0.00
	7	13	2.03	-119.8	5.49	1318 \pm 42	13.6 \pm 0.2	-119.5 \pm 1.4	0.3 \pm 1.8	-35 \pm 123	-39 \pm 97	-0.03 \pm 0.11	-0.03 \pm 0.08
	8	14	3.04	-131.0	8.21	836 \pm 24	8.6 \pm 0.4	-134.6 \pm 1.6	3.6 \pm 1.9	86 \pm 36	34 \pm 36	0.12 \pm 0.05	0.05 \pm 0.05
	9	44	4.62	-127.5	12.48	900 \pm 7	9.3 \pm 0.1	-127.9 \pm 0.4	0.4 \pm 0.5	126 \pm 5	18 \pm 5	0.16 \pm 0.01	0.02 \pm 0.01
	10	16	1.12	-120.2	3.03	492 \pm 22	5.1 \pm 0.2	-118.6 \pm 2.1	1.6 \pm 2.4	230 \pm 33	17 \pm 26	0.54 \pm 0.08	0.04 \pm 0.06
	12	31	2.81	-135.2	7.59	939 \pm 18	9.7 \pm 0.2	-135.0 \pm 1.1	0.2 \pm 1.3	30 \pm 27	52 \pm 27	0.04 \pm 0.03	0.06 \pm 0.03
	15	17	2.11	-141.0	5.70	907 \pm 27	9.4 \pm 0.3	-140.1 \pm 1.7	0.9 \pm 1.8	206 \pm 58	-30 \pm 59	0.26 \pm 0.07	-0.04 \pm 0.07
1253-055	1	89	4.64	-122.1	29.28	359 \pm 2	11.4 \pm 0.1	-138.7 \pm 0.3	16.7 \pm 0.4	12 \pm 1	-2 \pm 1	0.05 \pm 0.01	-0.01 \pm 0.01
(3C 279)	2	34	3.34	-118.3	21.08	270 \pm 12	8.6 \pm 0.4	-113.2 \pm 1.9	5.1 \pm 1.9	-24 \pm 25	28 \pm 19	-0.14 \pm 0.14	0.16 \pm 0.11
	3	12	0.93	-126.4	5.87	220 \pm 19	7.0 \pm 0.6	-136.8 \pm 4.8	10.3 \pm 4.8	74 \pm 36	-101 \pm 36	0.52 \pm 0.25	-0.70 \pm 0.26
	5	76	2.44	-125.8	15.40	508 \pm 9	16.1 \pm 0.3	-126.5 \pm 1.0	0.7 \pm 1.1	-34 \pm 7	-11 \pm 7	-0.10 \pm 0.02	-0.03 \pm 0.02
	6	44	1.48	-127.2	9.34	486 \pm 10	15.4 \pm 0.3	-127.8 \pm 1.2	0.6 \pm 1.2	366 \pm 20	41 \pm 20	1.16 \pm 0.07	0.13 \pm 0.06
	7	28	1.42	-125.5	8.96	651 \pm 25	20.6 \pm 0.8	-120.8 \pm 1.9	4.8 \pm 2.0	27 \pm 64	48 \pm 56	0.06 \pm 0.15	0.11 \pm 0.13
	8	15	0.91	-135.0	5.74	289 \pm 18	9.2 \pm 0.6	-111.1 \pm 3.1	23.9 \pm 3.2	361 \pm 67	197 \pm 60	1.92 \pm 0.37	1.05 \pm 0.32
	10	11	0.78	-140.9	4.92	475 \pm 15	15.1 \pm 0.5	-136.7 \pm 1.7	4.2 \pm 1.9	-97 \pm 37	23 \pm 37	-0.31 \pm 0.12	0.07 \pm 0.12
1308+326	2	37	2.96	-73.0	23.79	399 \pm 13	20.8 \pm 0.7	-71.5 \pm 1.1	1.5 \pm 1.2	-8 \pm 7	10 \pm 5	-0.04 \pm 0.04	0.05 \pm 0.02
	3	12	1.70	-63.7	13.66	443 \pm 48	23.1 \pm 2.5	-75.8 \pm 3.5	12.1 \pm 3.6	128 \pm 74	-86 \pm 45	0.58 \pm 0.34	-0.39 \pm 0.21
	4	21	1.85	-51.7	14.87	519 \pm 22	27.1 \pm 1.1	-64.6 \pm 1.5	12.8 \pm 1.6	-39 \pm 40	18 \pm 24	-0.15 \pm 0.15	0.07 \pm 0.09
	5	34	2.09	-42.1	16.80	449 \pm 6	23.4 \pm 0.3	-46.2 \pm 0.8	4.1 \pm 0.9	-65 \pm 6	-17 \pm 6	-0.29 \pm 0.03	-0.08 \pm 0.03
	7	13	1.65	-61.6	13.26	428 \pm 18	22.3 \pm 0.9	-64.9 \pm 2.5	3.3 \pm 2.6	316 \pm 55	-46 \pm 57	1.47 \pm 0.26	-0.22 \pm 0.26
	9	19	0.45	-34.3	3.62	188 \pm 5	9.8 \pm 0.3	-43.4 \pm 1.5	9.1 \pm 1.6	36 \pm 8	-11 \pm 7	0.38 \pm 0.08	-0.11 \pm 0.08
1510-089	1	18	3.22	-25.4	16.10	713 \pm 17	15.9 \pm 0.4	-25.7 \pm 0.8	0.3 \pm 0.9	-95 \pm 22	-3 \pm 13	-0.18 \pm 0.04	-0.01 \pm 0.03
	4	10	2.04	-34.9	10.20	909 \pm 52	20.3 \pm 1.2	-33.7 \pm 3.6	1.2 \pm 4.0	88 \pm 89	-11 \pm 100	0.13 \pm 0.13	-0.02 \pm 0.15
1546+027	3	12	2.49	172.4	13.59	406 \pm 27	10.3 \pm 0.7	169.1 \pm 1.2	3.4 \pm 1.3	2 \pm 27	-18 \pm 6	0.01 \pm 0.09	-0.06 \pm 0.02
	4	11	1.12	1									

Table 1
(Continued)

Source	I.D.	N	$\langle R \rangle$ (mas)	$\langle \vartheta \rangle$ (deg.)	d_{proj} (pc)	μ ($\mu\text{as yr}^{-1}$)	β_{obs}	ϕ (deg.)	$ \langle \vartheta \rangle - \phi $ (deg.)	$\dot{\mu}_{\parallel}$ ($\mu\text{as yr}^{-2}$)	$\dot{\mu}_{\perp}$ ($\mu\text{as yr}^{-2}$)	$\dot{\eta}_{\parallel}$	$\dot{\eta}_{\perp}$
(1)	(2)	(3)	(4)	(5)	(6)	(7)	(8)	(9)	(10)	(11)	(12)	(13)	(14)
1637+574	1	12	4.31	-159.3	31.67	212 \pm 9	8.9 \pm 0.4	-149.2 \pm 2.6	10.1 \pm 2.6	-29 \pm 8	12 \pm 8	-0.24 \pm 0.07	0.10 \pm 0.07
1641+399	2	28	5.49	-77.3	36.44	239 \pm 14	8.3 \pm 0.5	-57.9 \pm 3.6	19.4 \pm 3.6	-34 \pm 9	11 \pm 9	-0.23 \pm 0.06	0.07 \pm 0.06
(3C 345)	3	32	3.33	-90.8	22.10	320 \pm 10	11.1 \pm 0.3	-73.5 \pm 1.4	17.3 \pm 1.4	4 \pm 6	44 \pm 5	0.02 \pm 0.03	0.22 \pm 0.02
	6	34	2.47	-90.9	16.39	342 \pm 5	11.8 \pm 0.2	-84.7 \pm 0.6	6.2 \pm 0.6	-1 \pm 3	9 \pm 2	-0.01 \pm 0.02	0.04 \pm 0.01
	7	35	2.30	-97.1	15.26	374 \pm 4	12.9 \pm 0.1	-92.1 \pm 0.9	5.0 \pm 1.0	6 \pm 3	9 \pm 4	0.02 \pm 0.01	0.04 \pm 0.02
	8	30	1.68	-88.8	11.15	325 \pm 4	11.2 \pm 0.1	-87.3 \pm 0.8	1.5 \pm 0.9	19 \pm 3	-11 \pm 3	0.09 \pm 0.01	-0.05 \pm 0.02
	9	27	1.53	-93.7	10.15	348 \pm 9	12.0 \pm 0.3	-98.8 \pm 0.8	5.1 \pm 0.8	4 \pm 7	-13 \pm 4	0.02 \pm 0.03	-0.06 \pm 0.02
	11	18	0.98	-86.8	6.50	559 \pm 15	19.3 \pm 0.5	-87.8 \pm 0.7	1.0 \pm 0.8	73 \pm 35	-16 \pm 19	0.21 \pm 0.10	-0.05 \pm 0.05
	12	15	1.10	-88.8	7.30	471 \pm 27	16.3 \pm 0.9	-86.1 \pm 1.4	2.7 \pm 1.7	-149 \pm 57	31 \pm 31	-0.50 \pm 0.20	0.10 \pm 0.10
1655+077	6	11	1.83	-34.4	12.41	312 \pm 12	11.2 \pm 0.4	-40.8 \pm 2.1	6.4 \pm 2.4	14 \pm 9	-5 \pm 9	0.08 \pm 0.05	-0.03 \pm 0.05
1730-130	2	16	6.89	14.6	53.87	466 \pm 27	22.5 \pm 1.3	15.6 \pm 2.4	1.0 \pm 2.5	-37 \pm 15	-11 \pm 11	-0.15 \pm 0.06	-0.04 \pm 0.05
	6	15	1.86	27.3	14.54	324 \pm 10	15.7 \pm 0.5	25.6 \pm 1.2	1.7 \pm 1.4	13 \pm 7	-8 \pm 5	0.08 \pm 0.04	-0.05 \pm 0.03
1749+096	5	22	0.41	-2.2	1.90	121 \pm 18	2.4 \pm 0.4	22.2 \pm 4.2	24.4 \pm 4.3	140 \pm 36	21 \pm 18	1.53 \pm 0.45	0.23 \pm 0.20
1800+440	3	11	4.44	-162.5	31.01	407 \pm 13	15.4 \pm 0.5	-160.6 \pm 2.4	1.9 \pm 2.5	-5 \pm 9	1 \pm 11	-0.02 \pm 0.04	0.01 \pm 0.05
1823+568	1	14	7.60	-160.9	53.11	248 \pm 51	9.4 \pm 1.9	-170.8 \pm 4.9	9.9 \pm 4.9	34 \pm 58	-6 \pm 24	0.23 \pm 0.39	-0.04 \pm 0.16
	4	28	3.90	-158.7	27.25	550 \pm 13	20.9 \pm 0.5	-162.6 \pm 1.2	3.9 \pm 1.3	-16 \pm 12	-24 \pm 8	-0.05 \pm 0.04	-0.07 \pm 0.03
	6	13	1.84	-161.8	12.86	152 \pm 11	5.8 \pm 0.4	-164.8 \pm 3.4	3.0 \pm 3.4	-40 \pm 26	52 \pm 20	-0.44 \pm 0.29	0.57 \pm 0.22
	12	22	1.97	-161.4	13.77	88 \pm 7	3.3 \pm 0.3	-153.7 \pm 4.6	7.7 \pm 4.7	-7 \pm 10	-25 \pm 9	-0.14 \pm 0.19	-0.46 \pm 0.18
1828+487 (3C 380)	2	12	11.86	-34.8	84.34	322 \pm 9	12.6 \pm 0.3	-37.9 \pm 1.3	3.1 \pm 1.3	-4 \pm 7	-1 \pm 6	-0.02 \pm 0.04	-0.00 \pm 0.03
	3	12	10.75	-31.8	76.45	266 \pm 3	10.4 \pm 0.1	-38.2 \pm 0.7	6.4 \pm 0.7	4 \pm 2	-13 \pm 3	0.02 \pm 0.01	-0.08 \pm 0.02
	5	12	5.12	-28.4	36.41	348 \pm 10	13.7 \pm 0.4	-26.1 \pm 1.1	2.2 \pm 1.1	13 \pm 7	5 \pm 5	0.06 \pm 0.03	0.02 \pm 0.02
	6	11	2.50	-29.3	17.78	321 \pm 11	12.6 \pm 0.4	-31.8 \pm 1.5	2.5 \pm 1.6	-16 \pm 9	-5 \pm 7	-0.08 \pm 0.05	-0.03 \pm 0.04
	8	10	2.05	-38.4	14.58	310 \pm 6	12.2 \pm 0.2	-38.1 \pm 0.9	0.2 \pm 0.9	18 \pm 4	3 \pm 4	0.10 \pm 0.02	0.02 \pm 0.02
1928+738 (4C +73.18)	1	32	11.70	166.8	51.98	447 \pm 18	8.5 \pm 0.3	-180.0 \pm 0.9	13.2 \pm 0.9	-11 \pm 10	3 \pm 4	-0.03 \pm 0.03	0.01 \pm 0.01
	2	12	6.32	165.2	28.08	384 \pm 58	7.3 \pm 1.1	172.7 \pm 3.8	7.5 \pm 3.8	-63 \pm 68	-4 \pm 31	-0.21 \pm 0.23	-0.02 \pm 0.11
	3	32	4.56	163.5	20.26	227 \pm 11	4.3 \pm 0.2	174.0 \pm 1.8	10.5 \pm 1.8	9 \pm 6	1 \pm 4	0.05 \pm 0.03	0.00 \pm 0.02
	4	10	3.56	170.8	15.81	328 \pm 27	6.2 \pm 0.5	173.8 \pm 1.8	3.0 \pm 1.8	113 \pm 66	31 \pm 28	0.45 \pm 0.26	0.12 \pm 0.11
	5	30	3.12	170.4	13.86	281 \pm 12	5.3 \pm 0.2	167.4 \pm 0.9	2.9 \pm 0.9	-11 \pm 7	-7 \pm 3	-0.05 \pm 0.03	-0.03 \pm 0.01
	6	28	2.64	159.7	11.73	256 \pm 4	4.9 \pm 0.1	171.8 \pm 0.7	12.1 \pm 0.8	-15 \pm 3	28 \pm 2	-0.08 \pm 0.01	0.14 \pm 0.01
	8	32	1.82	157.4	8.09	271 \pm 4	5.2 \pm 0.1	163.5 \pm 0.4	6.1 \pm 0.5	7 \pm 2	5 \pm 1	0.04 \pm 0.01	0.02 \pm 0.01
	9	28	1.42	151.5	6.31	246 \pm 8	4.7 \pm 0.1	151.3 \pm 1.3	0.2 \pm 1.5	4 \pm 5	2 \pm 4	0.02 \pm 0.03	0.01 \pm 0.02
	10	23	1.02	156.7	4.53	212 \pm 7	4.0 \pm 0.1	153.2 \pm 1.7	3.6 \pm 1.9	24 \pm 5	-3 \pm 5	0.15 \pm 0.03	-0.02 \pm 0.03
	11	22	0.64	157.9	2.84	134 \pm 4	2.5 \pm 0.1	156.1 \pm 1.4	1.8 \pm 1.7	-8 \pm 4	3 \pm 3	-0.08 \pm 0.03	0.03 \pm 0.03
	1957+405 (Cygnus A)	3	21	2.32	-79.4	2.49	57 \pm 9	0.2 \pm 0.0	-90.0 \pm 3.0	10.6 \pm 3.0	-22 \pm 5	-4 \pm 2	-0.40 \pm 0.12
2021+614	4	21	1.54	-81.8	1.66	55 \pm 9	0.2 \pm 0.0	-95.5 \pm 3.9	13.7 \pm 4.0	-13 \pm 4	-3 \pm 2	-0.24 \pm 0.09	-0.06 \pm 0.04
	6	21	0.89	-82.4	0.96	45 \pm 5	0.2 \pm 0.0	-100.1 \pm 4.0	17.7 \pm 4.1	1 \pm 3	1 \pm 2	0.02 \pm 0.08	0.03 \pm 0.04
	4	18	0.58	24.0	2.09	29 \pm 3	0.4 \pm 0.0	0.0 \pm 3.6	24.0 \pm 3.7	-8 \pm 2	-6 \pm 1	-0.32 \pm 0.10	-0.26 \pm 0.06
2121+053	2	10	1.01	-69.8	8.58	163 \pm 7	13.1 \pm 0.6	-56.4 \pm 2.8	13.4 \pm 3.1	18 \pm 5	12 \pm 6	0.33 \pm 0.09	0.21 \pm 0.10
2128-123	3	10	5.52	-148.4	33.61	228 \pm 5	6.8 \pm 0.1	-160.6 \pm 0.6	12.2 \pm 0.6	-32 \pm 5	14 \pm 2	-0.21 \pm 0.03	0.09 \pm 0.02
2131-021	1	13	1.56	101.5	13.15	192 \pm 12	12.0 \pm 0.8	100.0 \pm 3.1	1.5 \pm 3.3	0 \pm 9	17 \pm 6	0.00 \pm 0.10	0.21 \pm 0.07
	3	10	1.58	114.0	13.32	222 \pm 5	13.8 \pm 0.3	97.0 \pm 3.0	17.1 \pm 3.1	6 \pm 9	-67 \pm 21	0.07 \pm 0.10	-0.69 \pm 0.21
	4	13	0.86	98.5	7.25	83 \pm 4	5.2 \pm 0.2	78.8 \pm 3.1	19.6 \pm 3.2	-8 \pm 3	2 \pm 5	-0.23 \pm 0.09	0.06 \pm 0.14
2134+004	2	29	1.74	-67.7	14.79	73 \pm 5	5.9 \pm 0.4	-145.7 \pm 3.6	78.0 \pm 3.7	-11 \pm 3	7 \pm 3	-0.44 \pm 0.13	0.30 \pm 0.12
2136+141	3	11	0.83	-89.5	6.84	59 \pm 2	5.4 \pm 0.2	-132.8 \pm 2.3	43.2 \pm 2.4	-8 \pm 1	-6 \pm 1	-0.47 \pm 0.08	-0.34 \pm 0.08
	4	14	0.53	-71.6	4.37	39 \pm 2	3.5 \pm 0.2	-126.1 \pm 2.8	54.6 \pm 2.9	-5 \pm 1	-3 \pm 1	-0.40 \pm 0.10	-0.28 \pm 0.11
2145+067	2	17	0.74	124.0	5.94	42 \pm 3	2.2 \pm 0.2	127.0 \pm 4.5	3.0 \pm 4.6	1 \pm 2	-3 \pm 2	0.03 \pm 0.10	-0.14 \pm 0.11
	3	12	0.41	113.9	3.29	48 \pm 2	2.5 \pm 0.1	146.4 \pm 2.6	32.5 \pm 2.9	1 \pm 2	-2 \pm 2	0.02 \pm 0.09	-0.09 \pm 0.08
2200+420 (BL Lac)	1	10	4.76	174.8	6.17	2341 \pm 163	10.7 \pm 0.8	150.8 \pm 3.1	24.1 \pm 3.2	-212 \pm 688	-343 \pm 540	-0.10 \pm 0.31	-0.16 \pm 0.25
	2	23	4.75	173.1	6.15	1595 \pm 83	7.3 \pm 0.4	155.3 \pm 3.0	17.8 \pm 3.3	-189 \pm 155	-334 \pm 164	-0.13 \pm	

Table 1
(Continued)

Source	I.D.	N	$\langle R \rangle$ (mas)	$\langle \vartheta \rangle$ (deg.)	d_{proj} (pc)	μ ($\mu\text{as yr}^{-1}$)	β_{obs}	ϕ (deg.)	$ \langle \vartheta \rangle - \phi $ (deg.)	$\dot{\mu}_{\parallel}$ ($\mu\text{as yr}^{-2}$)	$\dot{\mu}_{\perp}$ ($\mu\text{as yr}^{-2}$)	$\dot{\eta}_{\parallel}$	$\dot{\eta}_{\perp}$
(1)	(2)	(3)	(4)	(5)	(6)	(7)	(8)	(9)	(10)	(11)	(12)	(13)	(14)
2223–052 (3C 446)	1	14	5.29	97.6	44.99	219 ± 19	14.5 ± 1.3	89.2 ± 3.3	8.4 ± 3.3	16 ± 22	-3 ± 15	0.17 ± 0.24	-0.04 ± 0.16
	2	22	3.14	103.4	26.71	86 ± 8	5.7 ± 0.5	94.1 ± 3.5	9.3 ± 3.5	-7 ± 4	6 ± 2	-0.20 ± 0.11	0.17 ± 0.07
	4	18	0.73	86.9	6.21	260 ± 7	17.2 ± 0.5	111.6 ± 1.3	24.7 ± 1.7	37 ± 6	34 ± 5	0.34 ± 0.06	0.31 ± 0.05
	5	10	0.59	105.1	5.02	218 ± 15	14.4 ± 1.0	90.7 ± 3.2	14.4 ± 4.1	25 ± 16	-11 ± 14	0.27 ± 0.18	-0.12 ± 0.16
2230+114 (CTA 102)	2	20	10.95	157.6	88.83	173 ± 12	9.3 ± 0.6	137.2 ± 4.0	20.4 ± 4.0	-1 ± 10	-3 ± 10	-0.01 ± 0.11	-0.04 ± 0.11
	7	12	2.75	150.7	22.31	181 ± 28	9.7 ± 1.5	175.4 ± 2.8	24.8 ± 3.0	-9 ± 21	25 ± 7	-0.10 ± 0.23	0.28 ± 0.09
	9	18	1.17	132.9	9.49	161 ± 10	8.6 ± 0.5	144.3 ± 3.6	11.4 ± 3.7	-30 ± 9	3 ± 10	-0.38 ± 0.12	0.04 ± 0.12
2243–123	2	11	3.59	19.9	24.54	151 ± 9	5.5 ± 0.3	37.7 ± 3.6	17.8 ± 3.7	1 ± 6	-0 ± 7	0.01 ± 0.07	-0.00 ± 0.07
	3	11	1.86	-1.4	12.72	121 ± 5	4.4 ± 0.2	7.8 ± 0.6	9.3 ± 0.6	13 ± 3	1 ± 1	0.17 ± 0.05	0.01 ± 0.01
2251+158 (3C 454.3)	2	53	5.87	-80.7	45.21	84 ± 4	3.9 ± 0.2	-37.1 ± 3.2	43.7 ± 3.3	-9 ± 3	-4 ± 3	-0.19 ± 0.06	-0.10 ± 0.06
	3	12	2.61	-82.9	20.10	163 ± 15	7.6 ± 0.7	-37.0 ± 5.0	46.0 ± 5.0	85 ± 44	-145 ± 43	0.97 ± 0.51	-1.66 ± 0.51
	4	33	2.00	-106.0	15.40	304 ± 17	14.2 ± 0.8	-109.6 ± 2.9	3.5 ± 3.0	29 ± 24	-57 ± 19	0.18 ± 0.15	-0.35 ± 0.12
	5	49	1.58	-36.1	12.17	128 ± 8	6.0 ± 0.4	-41.0 ± 3.3	4.9 ± 3.4	14 ± 5	-31 ± 4	0.21 ± 0.07	-0.46 ± 0.07
	8	18	0.50	-89.8	3.85	291 ± 9	13.6 ± 0.4	-95.6 ± 1.3	5.7 ± 1.4	-350 ± 41	-107 ± 32	-2.23 ± 0.27	-0.68 ± 0.21
	11	34	0.90	-93.2	6.93	120 ± 9	5.6 ± 0.4	-92.5 ± 3.1	0.8 ± 3.1	85 ± 16	-6 ± 11	1.31 ± 0.26	-0.09 ± 0.17
2345–167	1	12	3.34	120.1	21.86	400 ± 24	13.5 ± 0.8	115.1 ± 1.8	5.0 ± 2.1	-8 ± 16	3 ± 9	-0.03 ± 0.06	0.01 ± 0.03

Notes. Columns are as follows: (1) Source name in B1950 coordinates (Alternate source name); (2) Component ID; (3) Number of epochs; (4) Mean radial separation from core in milliarcseconds (averaged over all epochs); (5) Mean structural position angle in degrees; (6) Mean projected radial distance in parsecs; (7) Angular proper motion in microarcseconds per year; (8) Apparent speed in units of the speed of light; (9) Proper motion position angle in degrees; (10) Absolute difference between mean structural position angle and proper motion position angle in degrees; (11) Angular acceleration parallel to the proper motion position angle in microarcseconds per year per year; (12) Angular acceleration perpendicular to the proper motion position angle in microarcseconds per year per year; (13) Relative parallel acceleration as defined in Section 3.3; (14) Relative perpendicular acceleration as defined in Section 3.3.

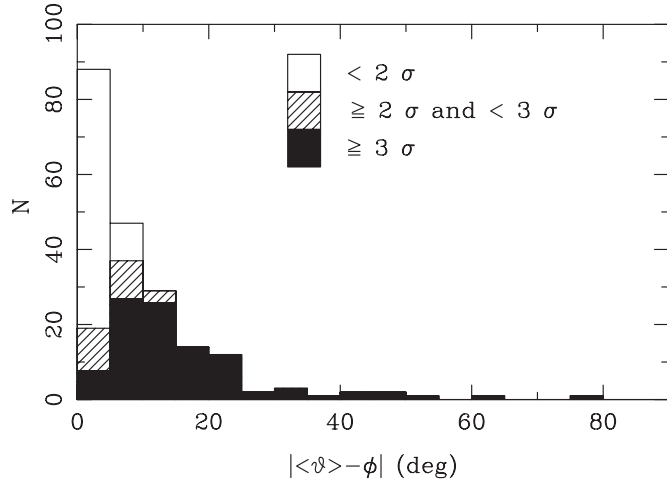


Figure 3. Distribution of velocity vector alignment parameter, $|\langle \vartheta \rangle - \phi|$, for the 203 jet components in our restricted sample. Hash and solid fill styles indicate non-radial motion, $|\langle \vartheta \rangle - \phi| > 0$, significant at the 2σ – 3σ and $\geq 3\sigma$ levels, respectively.

which are robustly larger than 0.1, corresponding to a 10% change in the apparent vector velocity per year in our frame. We find that 51 components have high parallel accelerations and 29 have high perpendicular accelerations with magnitudes that are at least 2σ above 0.1.

Figure 4 shows histograms of the magnitudes of all the relative acceleration measurements parallel, $\dot{\eta}_{\parallel}$, and perpendicular, $\dot{\eta}_{\perp}$, to the apparent component motion. The distribution of relative parallel accelerations is much broader than the distribution of relative perpendicular accelerations, and a Kolmogorov–Smirnov (K–S) test gives a probability of only $P < 0.001$ that they are drawn from the same distribution. The relative parallel accelerations have an average magnitude of 0.25 while the perpendicular accelerations average only 0.15. We find that

this difference between parallel and perpendicular accelerations remains highly significant whether we divide our sample to only look at nearby sources with redshifts of $z < 0.1$ or only more distant sources with $z > 0.1$. These differences are also highly significant whether or not we include components at mean angular separations $\langle R \rangle < 2.0$ mas, which appear to have less well determined accelerations (see below).

One possible complicating factor is that there might be a greater uncertainty in parallel accelerations as those accelerations are taken along the component motion which tends to be along the jet direction. Along the jet direction there is greater opportunity for confusion from nearby components just up or downstream as well as jitter in the measured core position along the jet direction due to the emergence of new features. We find a marginally significant difference between the distributions of uncertainties for the parallel and perpendicular accelerations with a K–S test giving a probability $P = 0.055$ that they are drawn from the same distribution. However, this marginal difference in uncertainties between the parallel and perpendicular accelerations does not appear to drive the difference in the magnitudes of the measured accelerations. Indeed, if we only examine components with uncertainties in their parallel and perpendicular accelerations which differ by less than 10%, we find that the difference in magnitude between the parallel and perpendicular accelerations remains significant with $P = 0.013$ and mean values of 0.23 and 0.15 respectively.

Figure 5 plots relative parallel and perpendicular accelerations versus average radial position, $\langle R \rangle$, from the base of the jet in milliarcseconds. There appears to be little overall relation between average radial position and relative acceleration, although components at less than 2 mas from the base of the jet appear to have a larger spread in the magnitudes as well as larger uncertainties for both their relative parallel and perpendicular accelerations. K–S tests on these quantities show significant differences between the distributions for the compo-

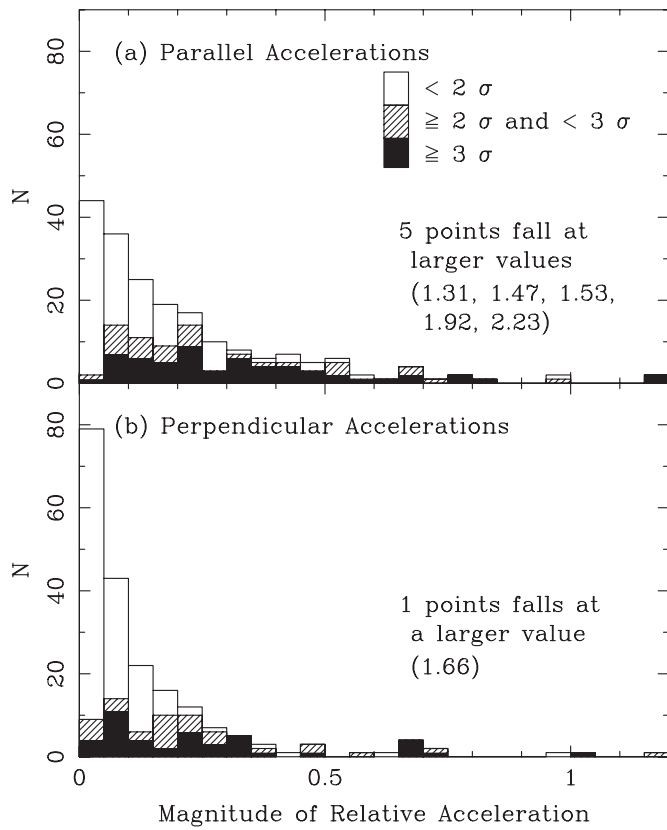


Figure 4. Histograms of magnitudes of relative accelerations, parallel, $\dot{\eta}_{\parallel}$ (panel (a)), and perpendicular, $\dot{\eta}_{\perp}$ (panel (b)), to the apparent component motion. Hash and solid fill styles indicated angular acceleration significant at the 2σ – 3σ and $\geq 3\sigma$ levels, respectively. As indicated, five parallel accelerations and one perpendicular acceleration lie to the right of the plot.

nents at $\langle R \rangle < 2$ mas compared to those at ≥ 2 milliarcseconds with $P \leq 0.001$ in each case. This result suggests that components that spent a significant fraction of their time within a few beam-widths of the base of the jet may have accelerations which are less well determined than those at large angular radii, perhaps due to confusion from closely spaced components in the core region and/or the core itself.

Figures 6 and 7 plot relative parallel and perpendicular accelerations versus the average projected linear distance, $d_{\text{proj}} = D_A \langle R \rangle$, for a component, where D_A is the angular size distance to the host galaxy. Figure 7 includes only those components at $\langle R \rangle \geq 2$ mas. In Figure 6, there appears to be a decreasing spread in the magnitudes of accelerations at larger projected distances; however, this trend mostly disappears when the components at small angular separations are excluded in Figure 7.

The relative parallel accelerations in Figure 7 appear to show a bias toward positive accelerations at projected distances of $\lesssim 15$ pc and a bias toward negative accelerations at larger projected distances. These biases also appear in Figure 6 but with more scatter.

To investigate further the relationship between sign of the apparent parallel acceleration and projected linear distance, Figure 8 contains histograms of the projected linear distances of components with positive and negative parallel acceleration. These histograms contain only the $N = 64$ components which have $\geq 3\sigma$ parallel angular accelerations so that we may be confident of the sign of the acceleration. A K–S test shows a significant difference between the linear distance distributions of the positively and negatively accelerating components, whether

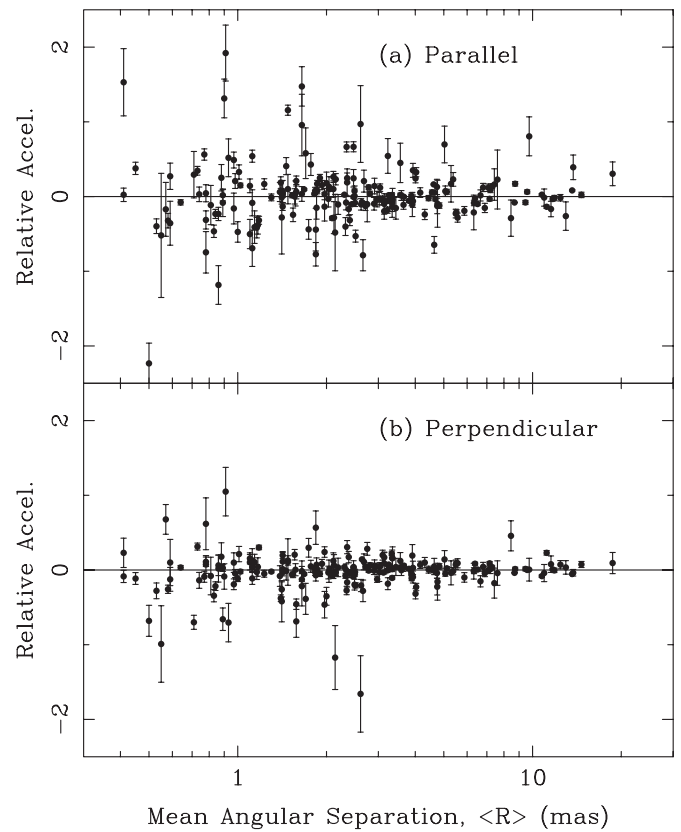


Figure 5. Relative accelerations, parallel, $\dot{\eta}_{\parallel}$ (panel (a)), and perpendicular, $\dot{\eta}_{\perp}$ (panel (b)), to the apparent component motion plotted against average radial distance of the component from the core position in milliarcseconds.

we consider all components: $P = 0.013$ with mean linear distances of 9.1 and 17.1 parsecs for the positively and negatively accelerating components respectively, or we consider only components at mean angular distances $\langle R \rangle \geq 2.0$ mas, where we find $P = 0.003$ with mean linear distances of 10.4 and 24.0 parsecs for the positive and negatively accelerating components, respectively. If we limit the analysis to jets at larger redshifts of $z > 0.1$, we also find a significant difference between the linear distance distributions of positively and negatively accelerating components, with $P = 0.023$ and mean linear distances of 10.9 and 18.8 parsecs for the positive and negative components respectively.

If we further limit the larger redshift, $z > 0.1$, sample to components at $\langle R \rangle \geq 2.0$ mas, we have too few components (seven positive accelerations, 15 negative) to reliably detect a difference between their linear distance distributions ($P = 0.14$ with means of 18.2 and 28.5 parsecs for the positive and negative components respectively); however, if we allow $\geq 2\sigma$ parallel angular accelerations to contribute to the test, we do find a significant difference between the populations with $P = 0.013$ that they are drawn from the same distribution with means of 16.7 and 28.3 parsecs linear distance for the positive and negative components respectively. Indeed, including the $\geq 2\sigma$ parallel angular accelerations in all of the above tests of the linear distance distributions increases the overall sample from $N = 64$ to $N = 96$ components and reduces the P -value in each test, improving our confidence that the linear distances for the positive and negative parallel accelerations are drawn from different distributions.

No similar bias between positive and negative perpendicular accelerations appears in Figures 6 and 7, and a K–S test on

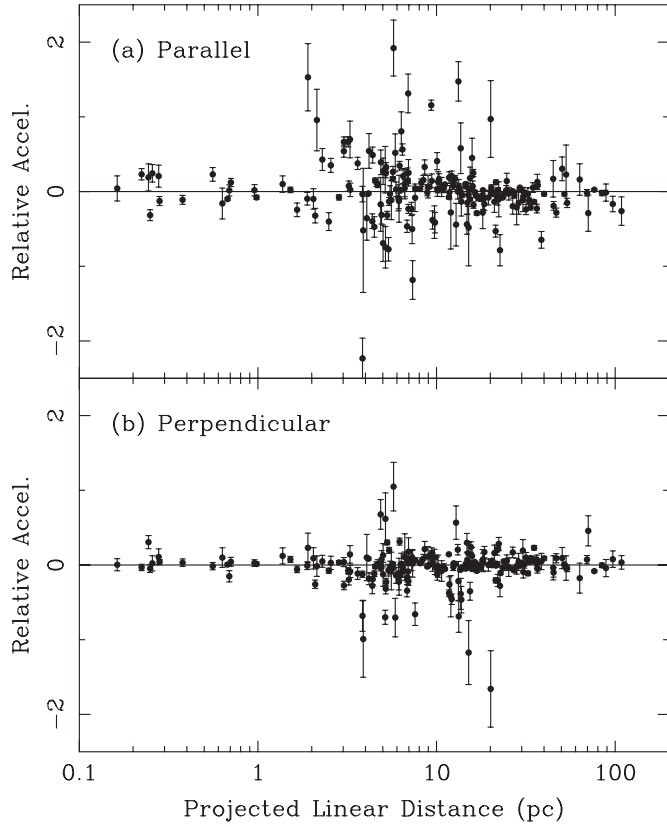


Figure 6. Relative accelerations, parallel, $\dot{\eta}_{\parallel}$ (panel (a)), and perpendicular, $\dot{\eta}_{\perp}$ (panel (b)), to the apparent component motion plotted against average projected linear distance of the component from the core position in parsecs. All components with an projected linear distance of ≤ 1.0 pc are from 0238–084 (NGC 1052) at $z = 0.005$.

the linear distance distributions for components which have $\geq 3\sigma$ perpendicular angular acceleration detects no difference between the positive and negative perpendicular accelerations: $P = 0.78$ with nearly identical means of 15.6 parsecs.

3.4. Connection Between Non-radial Motion and Acceleration

Figure 9 shows the $|\langle\vartheta\rangle - \phi|$ distributions for high-acceleration and low-acceleration components for both parallel and perpendicular accelerations. High- and low-acceleration components are defined as those with relative accelerations greater or less than 0.1 at a 2σ level. To isolate the relationship of either parallel or perpendicular acceleration to non-radial motion, components with high parallel acceleration are excluded from the perpendicular acceleration histograms (panels (b) and (d)), and likewise, components with high perpendicular acceleration are excluded from the parallel acceleration histograms (panels (a) and (c)). A K–S test finds no significant difference in the $|\langle\vartheta\rangle - \phi|$ distributions for parallel accelerations: $P = 0.12$ with mean values of $7^{\circ}.8$ and $9^{\circ}.6$ for the low and high parallel accelerating components, respectively. However, a K–S test does detect a highly significant difference between the distributions for perpendicular accelerations: $P = 0.004$ with mean values of $5^{\circ}.1$ and $12^{\circ}.6$ for the low and high perpendicular accelerations, respectively. These results indicate that strong perpendicular accelerations are linked with higher degrees of non-radial motion.

Figure 10, which plots the relative perpendicular acceleration, $\dot{\eta}_{\perp}$, versus the proper motion angle misalignment, $\langle\vartheta\rangle - \phi$, shows this relationship further. Note that here we have not taken

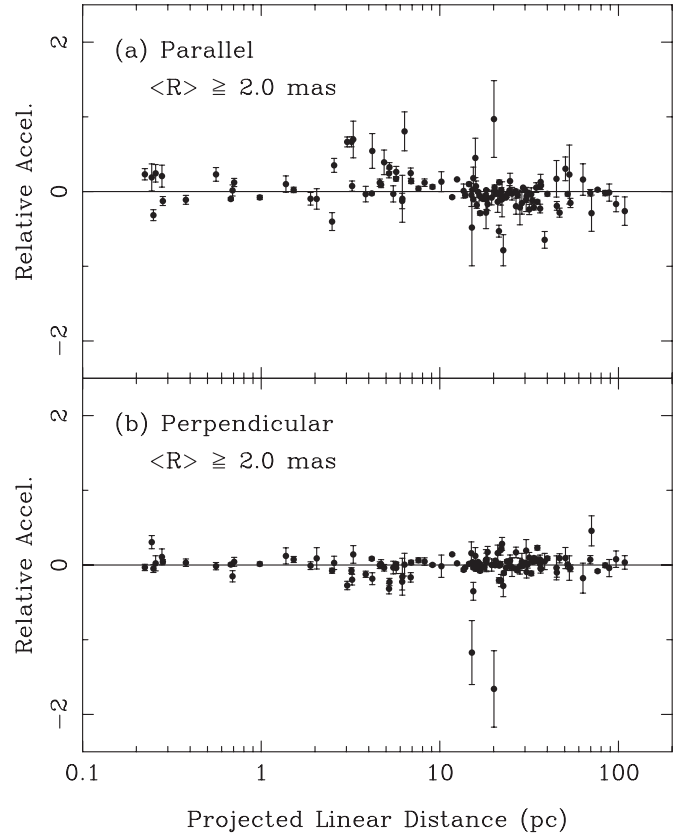


Figure 7. Relative accelerations, parallel, $\dot{\eta}_{\parallel}$ (panel (a)), and perpendicular, $\dot{\eta}_{\perp}$ (panel (b)), to the apparent component motion plotted against average projected linear distance of the component from the core position in parsecs. Only components with mean angular separations, $\langle R \rangle \geq 2.0$ mas are plotted here. All components with an projected linear distance of ≤ 1.0 pc are from 0238–084 (NGC 1052) at $z = 0.005$. Of the 29 components plotted between 1.0 and 10 parsecs, 19 are from either 3C 120 or Bllac at $z = 0.033$ and $z = 0.069$, respectively.

the absolute value of the misalignment angle so that we can compare the sign of the non-radial motion with the sign of the perpendicular acceleration. Figure 10 includes all 37 components from Table 1 which have both a significant non-radial motion and a significant perpendicular acceleration. We find that 30 of the 37 components have a perpendicular acceleration in the correct direction to produce the observed sign of the proper motion offset, i.e., with our sign definitions, a positive perpendicular acceleration in an originally radially moving component will eventually produce a negative misalignment. The probability of this agreement occurring by pure chance is extremely small ($P = 0.00015$). Figure 10 also shows a possible trend to larger accelerations for larger misalignments, although there are several exceptions.

4. DISCUSSION

In the previous section, we presented the results of our analysis of accelerations measured from 203 jet components from the MOJAVE sample. We reported and analyzed acceleration measurements both parallel and perpendicular to the apparent velocity. Parallel accelerations characterize changes in apparent speed of a component while perpendicular accelerations characterize changes in direction on the sky. We found significant angular accelerations parallel to the component velocities in about one-third of the sample, and about one-fifth had significant perpendicular accelerations. To facilitate comparison of

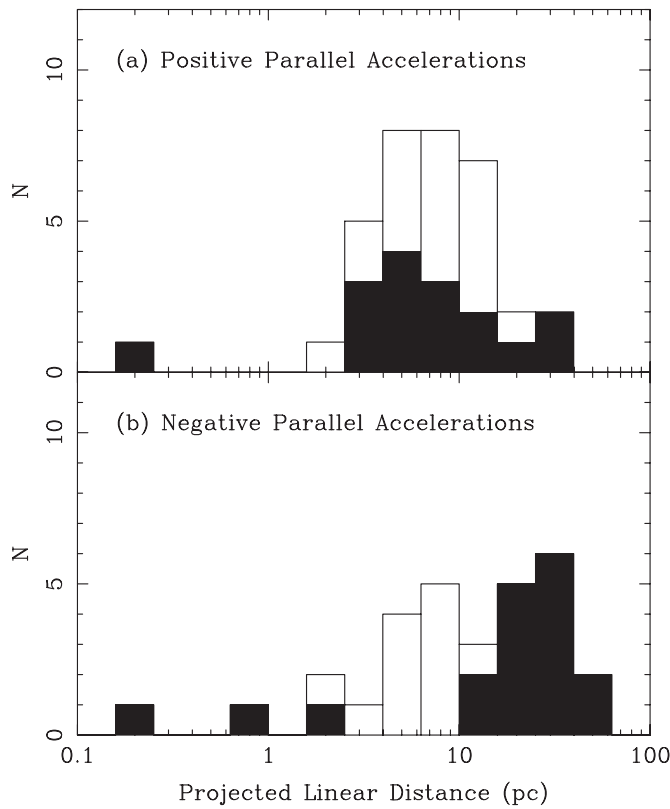


Figure 8. Histograms of projected linear distance for components with positive parallel accelerations (panel (a)) and negative parallel accelerations (panel (b)). Only components with angular accelerations significant at the $\geq 3\sigma$ level are plotted here. Components at mean angular separations $\langle R \rangle \geq 2.0$ mas are plotted as solid bars.

accelerations between different components and jets, we constructed relative accelerations, $\dot{\eta}_{\parallel}$ and $\dot{\eta}_{\perp}$, where we divide each acceleration by the apparent velocity of the component. As noted in Section 2, relative accelerations are also convenient for investigating rates of change of the intrinsic quantities that may lead to the observed accelerations.

4.1. Changes in Speed

Parallel accelerations, representing changes in apparent speed of a component or pattern, can be due either to intrinsic changes in the Lorentz factor, Γ , or angle to the line of sight, θ , see Section 2.1. Distinguishing between these possibilities in any individual case is difficult; however, we can begin by making the simple assumption that all observed accelerations are due only to changes in angle: θ and/or ϕ . Under this assumption, we showed in Section 2.2 that, averaged across many components and jets, we expect that, on average, the observed parallel accelerations would be about 60% of the magnitude of the observed perpendicular accelerations. However, this is not what we observed. We found that the distribution of parallel accelerations was much broader than the distribution of perpendicular accelerations with the mean parallel acceleration larger than the mean perpendicular acceleration by about a factor of 1.6.

Therefore, we infer that more than half of the magnitudes of the observed parallel accelerations can be attributed to intrinsic changes in the Lorentz factor, Γ , of the component or pattern. We emphasize that this is only an average statement, and that for any given component, we cannot be certain how much, if any, of the observed parallel acceleration is due to Lorentz factor versus intrinsic angle changes. We note, however, that for components

moving at the critical angle for maximal superluminal motion, $\cos \theta = \beta$, Equation (3) shows that any observed parallel acceleration must be due to changes in the Lorentz factor alone.

Given these results and the measurement of significant parallel accelerations in roughly a third of our sample, we conclude that changes in intrinsic speed are common. Whether these changes in component or pattern motion reflect underlying changes in the flow speed of the jet is not clear, and we discuss this issue further below.

Regarding the magnitudes of the parallel accelerations, in Section 3.3 we characterized a relative acceleration of >0.1 as high, corresponding to a more than 10% change in the component velocity during one year in our frame. We found that roughly a quarter ($N = 51$) of our components had relative parallel accelerations at least 2σ greater than 0.1, and a few components have much larger relative parallel accelerations: nine are greater than 0.5 at the 2σ level. If a jet component is moving with $\Gamma = \delta = 10$ and a relative parallel acceleration of 0.1, this corresponds to an intrinsic rate of change characterized by $\dot{\Gamma}/\Gamma = 10^{-3}$ per yr in the frame of the AGN host galaxy (see Section 2.1).

4.1.1. Relation with Linear Distance

As described in detail in Section 3.3, we found that components with positive parallel accelerations tended to appear at shorter linear distances from the jet core while components with negative parallel accelerations tended to appear at longer linear distances with means of approximately 10 and 20 parsecs, respectively. This trend can be seen most clearly in the histogram given in Figure 8 where the difference is strongest for those components at mean angular separations $\langle R \rangle \geq 2.0$ mas. We found that these differences persist even if we consider only jets at redshifts $z > 0.1$, eliminating a few nearby jets with several components at shorter projected distances.

While this trend is robust, positively accelerating components appear at shorter projected distances on average than negatively accelerating components, we note that there are many exceptions to the trend and no single source shows this clear pattern in several components all by itself. More typical for jets with multiple components is that some of the components show acceleration (either positive, negative, or both) and others do not. Given the arguments in the previous section, we expect that a significant fraction of these parallel accelerations reflect real changes in the Lorentz factor of the components or patterns; however, we do not know the extent to which they reflect changes in the underlying flow. If they do, then we may be seeing an overall trend for positive acceleration of the flow at shorter projected distances, $\lesssim 15$ parsecs, and negative acceleration of the flow at longer projected distances, $\gtrsim 15$ parsecs.

Quasar jets are observed to be at least mildly relativistic on scales of hundreds of kiloparsecs with beaming models of the observed jet and counterjet radio emission giving $\Gamma_{\text{kpc}} \simeq 1.3$ with values $\gtrsim 3$ being inconsistent with the data, suggesting at least some deceleration between parsec and kiloparsec scales (Wardle & Aaron 1997; Hardcastle et al. 1999; Mullin & Hardcastle 2009); however, the interpretation of X-ray emission observed on kiloparsec scales as inverse-Compton scattering from the cosmic microwave background seems to require $\Gamma_{\text{kpc}} \simeq 3\text{--}15$ (e.g., Sambruna et al. 2004).

If some jets begin decelerating on decaparsec scales, the rate of deceleration cannot remain at the relatively high values seen here. A jet component moving with $\Gamma = \delta = 10$ and an observed deceleration $\dot{\eta}_{\parallel} = -0.1$ will be experiencing a change

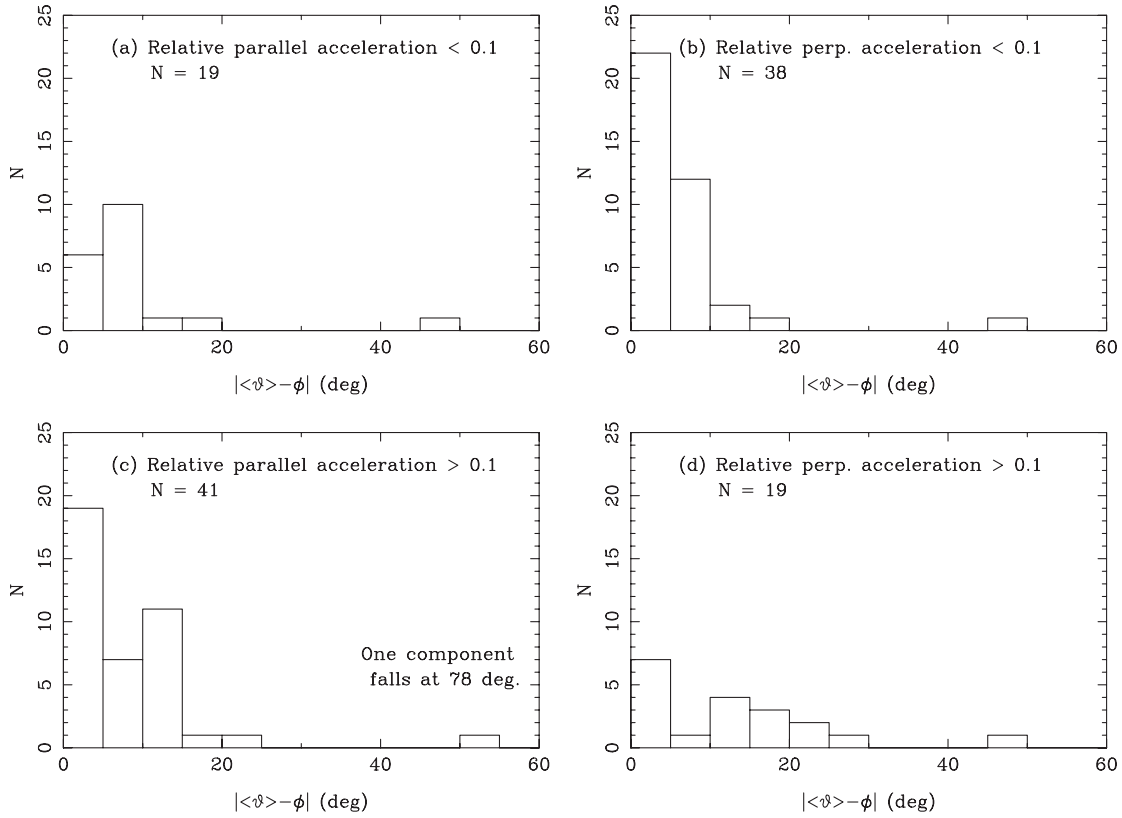


Figure 9. Histograms of velocity vector misalignments, $|\langle \vartheta \rangle - \phi|$, for jet components with low and high accelerations (top and bottom panels, respectively) either parallel or perpendicular to the component motion (left and right panels, respectively), as described in Section 3.4. Note that in panels (a) and (c), which plot parallel accelerations, components which also have high perpendicular accelerations are not included. Likewise, in panels (b) and (d), which plot perpendicular accelerations, components which also have high parallel accelerations are not included.

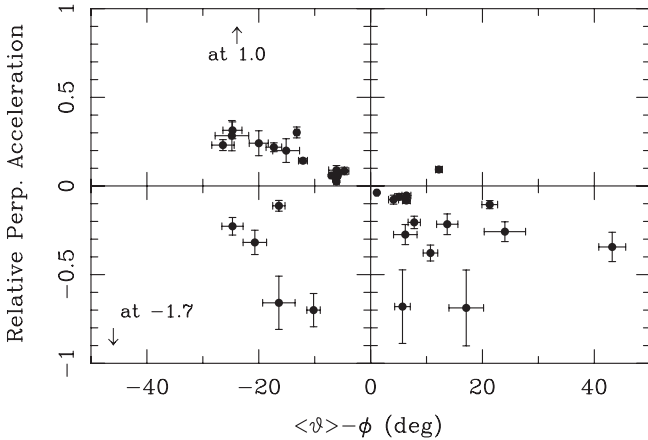


Figure 10. Plot of relative perpendicular acceleration versus $\langle \vartheta \rangle - \phi$ for all jet components with both significant non-radial motion and perpendicular acceleration in Table 1. Of the 37 components plotted here, 30 have opposite signs for their relative perpendicular accelerations and $\langle \vartheta \rangle - \phi$, indicating that the accelerations are in the correct direction to have produced the observed non-radial motion. Note that two points, indicated by arrows, have relative accelerations that fall above and below the plot at $+1.0$ and -1.7 , respectively.

in Lorentz factor characterized by $\dot{\Gamma}/\Gamma = -10^{-3}$ per yr in the rest frame of the host galaxy. If this rate remains constant, the component will decelerate to $\Gamma < 1.3$ in just 2000 years, long before it can travel hundreds of kiloparsecs.

4.1.2. Pattern Speed Versus Flow Speed

In Paper VI, we showed that the range of component speeds within an individual jet was much smaller than the range of

component speeds across our sample as a whole, indicating that individual jets do have a characteristic flow speed. However, in many cases, the range of speeds observed within individual jets was still reasonably large. In the sample of 203 component motions analyzed here, a range of speeds spanning a factor of two in an individual jet is not uncommon, and, in a few cases, there are larger differences. Taken together these result suggests that (1) pattern motion at a different speed than the underlying flow is a common feature of the component motion we are studying and that (2) the observed pattern motions do carry information about the underlying flow or we would see a much wider spread of apparent speed in individual jets. A key question is the extent to which the changes observed in component or pattern motions are reflective of changes in the underlying flow.

We noted above that the trend for components with increasing speed to be at smaller projected distances than components with decreasing speed was robust; however, there were many exceptions and individual jets did not show clear evidence of this pattern by themselves. These exceptions are consistent with some contribution from both random changes in pattern motion and changes in direction to the line of sight; however, the robustness of the overall trend suggests a common physical link. That link may be to the underlying flow, as suggested above, reflecting a tendency for positive acceleration of the flow speed at shorter projected distances, $\lesssim 15$ parsecs, and negative acceleration of the flow speed at longer projected distances, $\gtrsim 15$ parsecs. Alternatively, there may be common hydro-dynamical processes for shock propagation, such as the expectation that a leading shock will slowly decrease in apparent speed (Marscher & Gear 1985), which also play a role in producing this trend.

4.2. Changes in Direction

We characterized the “non-radial” motion for each component by its misalignment angle, the difference between the component’s structural position angle, $\langle\vartheta\rangle$, and its vector motion position angle, ϕ . Components with a misalignment angle of zero appear to be moving radially or ballistically, while those with significant misalignments must have changed their trajectory at some point. We found that significant non-radial motions were common, appearing in about half of our sample, and that large non-radial motions with misalignment angles robustly greater than 10° occur in about one-fifth of our sample. In general, the non-radial motions we observed were in the direction of the downstream jet, confirming the results of Kellermann et al. (2004) that while jet components may have different position angles, they ultimately tend to follow a pre-established flow direction rather than continue on ballistic trajectories. The degree to which this tendency results from jet collimation on parsec scales or simple bending of an already well collimated jet is unclear.

While the misalignment angles described above give an indication of whether a component has changed its trajectory in the past, they are not a direct measure of how much the component motion may have changed during our observations. However, the observed perpendicular accelerations for each component provide just such a direct measure of changes in direction of apparent component motion.

In Section 3.4, we showed there was a close connection between the observed perpendicular accelerations and the observed misalignment angles that characterize non-radial motion. We found that components with high perpendicular acceleration had a broader distribution of misalignment angles. We also examined components that had both a significant misalignment and a significant perpendicular acceleration, and we found the observed perpendicular acceleration had a strong tendency to be in the correct direction to have caused the observed misalignment angle. This is precisely what we would expect for a scenario in which components must have experienced some acceleration in the past to become non-radial.

4.3. Changes in Acceleration

As discussed briefly in Section 3 and in more detail in Paper VI, our proper motion model assumes a single, constant acceleration term for each of the x and y position coordinates in the sky. We then resolve these into accelerations parallel, $\dot{\mu}_{\parallel}$, and perpendicular, $\dot{\mu}_{\perp}$, to the observed velocity. The accelerations are fit relative to the middle epoch of a given component’s observations, and therefore represent the average accelerations experienced by the component throughout the period of observation.

With this approach, we are not sensitive to changes in acceleration, or “jerks,” that might be experienced by a component during our observations. A key example is the sudden change in speed and direction reported by Homan et al. (2003) in a strong component in 3C 279. During 1998, this component increased its apparent speed by more than 50% and changed its direction on the sky by $\sim 25^\circ$. Just prior to the change in direction, the component had a sharp rise in flux density and decrease in transverse size, and it had a steady decrease in flux density after the change (Homan et al. 2003). Zavala & Taylor (2001) also reported a change in polarization of the component associated with this change in direction. In the results reported here, this large, sudden change is just one part of a much longer trajectory

for this component (1253–055, component 1 in Table 1) spanning 89 VLBA epochs at 15 GHz since 1994. If we examine the trajectory from 1999 onward, after the sudden change, the remaining 77 epochs show significant parallel and perpendicular accelerations: $\dot{\mu}_{\parallel} = -5.6 \pm 1.7$ and $\dot{\mu}_{\perp} = +13.0 \pm 1.6 \mu\text{as yr}^{-2}$, which differ in sign and magnitude from the average values for the entire trajectory reported in Table 1.

Changes in accelerations of individual components might result not only from discrete, impulsive events, like that seen in 3C 279, but also from more gradual changes, perhaps as a component moves from a region of increasing flow speed to a region of decreasing flow speed. Our 89 epochs, spanning 13 years, on component 1 in 3C 279 represents an extreme example in temporal coverage of a single moving component. Improved time baselines on many other components may permit a larger study for changes in acceleration in individual components in the future. This issue might also be addressed with a detailed study examining changes in apparent velocity with other component properties such as flux density, polarization, and size, but that is beyond the scope of this work.

5. SUMMARY AND CONCLUSIONS

We have analyzed acceleration measurements for 203 jet components from the proper motions reported for the MOJAVE program in Paper VI. We have examined accelerations both parallel and perpendicular to the component velocity, representing changes in apparent speed and direction, respectively. Our main results are as follows.

1. We find significant parallel accelerations in roughly one third of our sample and significant perpendicular accelerations in about one fifth of our sample.
2. To compare accelerations between components moving with different apparent speeds, we define relative accelerations by taking the ratio $\dot{\beta}_{\text{obs}}/\beta_{\text{obs}}$. Defining high relative accelerations as those with magnitude >0.1 , corresponding to a 10% change in apparent velocity per year in our frame, we find that about one quarter of the components in our sample show high parallel accelerations and about one seventh have high perpendicular accelerations.
3. Changes in the apparent speed of components are due to changes in their Lorentz factor, as much or more so, than due to changes in their angle to the line of sight. This is evidenced by the fact that parallel accelerations have larger magnitudes on average than perpendicular accelerations. We estimate that more than half of the observed parallel accelerations are due to intrinsic changes in speed of the components or pattern.
4. On average, components with positive parallel accelerations, representing increasing apparent speed, are found closer to the jet base than components with negative parallel accelerations. While numerous exceptions to this trend are observed, perhaps due to the influence of pattern motion or directional changes, the overall trend itself is robust, suggesting a physical link between the observed pattern motions and the underlying flow. This trend may reflect a tendency for the jet flow to increase in speed on shorter length scales ($\lesssim 15$ pc projected) and decrease in speed at longer distances; however common hydrodynamical processes for shock propagation may also play a role in producing the observed trend.
5. Significant non-radial motions, characterized by a misalignment between a component’s structural position angle and

its velocity direction, appear in half of our sample with about one fifth showing significant misalignments greater than 10° . These misalignments have a strong tendency to be in the direction to better align the component motion with the downstream flow, confirming the results of Kellermann et al. (2004) that new jet components tend to follow a pre-established flow direction rather than continue on ballistic trajectories from the jet core.

6. Perpendicular accelerations appear to be closely linked with misalignment angles and are usually in the correct direction to have caused the observed misalignment.

Overall, the high incidence of accelerations and non-radial motions in our observations indicates that jet flows are still becoming organized on parsec to decaparsec scales. However, with a few exceptions, the observed changes, magnified by projection and apparent time compression, suggest only modest rates of change in intrinsic parameters on these length scales.

The authors wish to acknowledge the other members of the MOJAVE team. D.C.H. has been supported under NSF grant AST-0707693. M.L.L. has been supported under NSF grants AST-0406923 & AST-0807860, NASA-Fermi grant NNX08AV67G and a grant from the Purdue Research Foundation. T.S. has been supported in part by the Academy of Finland grant 120516. M.K. has been supported in part by an appointment to the NASA Postdoctoral Program at the Goddard Space Flight Center, administered by Oak Ridge Associated Universities through a contract with NASA. Part of this work was done by Y.Y.K. and T.S. during their Alexander von Humboldt fellowships at the MPIfR. Y.Y.K. is partly supported by the Russian Foundation for Basic Research (project 08-02-00545). This work has made use of data obtained from the National Radio Astronomy Observatory's Very Long Baseline Array and its public archive. The National Radio Astronomy Observatory is a facility of the National Science Foundation operated under cooperative agreement by Associated Universities, Inc. This research has made use of NASA's Astrophysics Data System, and the NASA/IPAC Extragalactic Database (NED). The latter is operated by the Jet Propulsion Laboratory, California Institute of Technology, under contract with the National Aeronautics and Space Administration.

APPENDIX

CHANGES IN APPARENT MOTION

This appendix complements Section 2 by presenting more detailed background and derivations of the relationships describing changes in apparent speed of parsec-scale AGN jet features observed in VLBI monitoring. This work builds upon the relationships laid out in Blandford & Königl (1979), and sources referenced therein. All of the relationships derived here apply strictly to the moving patterns that we see as features or “components” propagating in a jet. Intrinsically, a moving pattern has speed $= \beta c$ at angle θ to the line of sight. In principle, the flow of the jet may have a different speed, $\beta_f c$, and angle, θ_f ; however, beyond differences due to Doppler boosting, these values do not affect the apparent motions or changes in motion of the patterns. Here, we concern ourselves with pattern motion as the key observable. Note that for economy of notation, we have not applied a subscript to indicate the pattern quantities (β , Γ , θ , etc.) as additional subscripts are necessary for describing other aspects of the motion.

A.1. Basic Time Derivatives

We are interested in relating the rate of change of the observed angular speed, μ , to the intrinsic rates of change of the pattern speed (or equivalently, Lorentz factor) and angle to the line of sight. To make these comparisons, we first define the time frames involved and derivatives of the corresponding quantities.

We consider three time frames as follows.

1. Time, t , is taken to be the time in the host galaxy of the jet. This time does not include apparent time compression due to motion along the line of sight. It is the appropriate time for defining derivatives of the intrinsic quantities like Lorentz factor and angle to the line of sight.
2. We define the time t_{obs} to be the time frame in which events appear to unfold as seen along the direction of the observer in the host galaxy. This time does include apparent time compression due to motion along the line of sight, where $dt_{\text{obs}} = (1 - \beta \cos \theta) dt$.
3. We also define t'_{obs} to be the time in the frame of the observer in our galaxy, so $dt'_{\text{obs}} = (1 + z) dt_{\text{obs}}$.

With these time frames defined, we define the “dot” notation for derivatives to mean a time derivative with respect to the appropriate time frame for the quantity in question. Thus, we have the following definitions for time derivatives of the basic quantities:

$$\dot{\beta} = \frac{d\beta}{dt}, \quad (\text{A1})$$

$$\dot{\Gamma} = \frac{d\Gamma}{dt} = \dot{\beta} \Gamma^3, \quad (\text{A2})$$

$$\dot{\beta}_{\text{obs}} = \frac{d\beta_{\text{obs}}}{dt_{\text{obs}}}, \quad (\text{A3})$$

$$\dot{\mu} = \frac{d\mu}{dt'_{\text{obs}}} = \frac{d\mu}{dt_{\text{obs}}} (1 + z)^{-1}. \quad (\text{A4})$$

A.2. Vector Acceleration

To allow the possibility of changes in both the speed and direction of a jet feature's motion we consider the full vector acceleration, Equation (3) from Blandford & Königl (1979):

$$\frac{d\vec{\beta}_{\text{obs}}}{dt_{\text{obs}}} = (1 - \vec{\beta} \cdot \hat{n})^{-3} [(1 - \vec{\beta} \cdot \hat{n}) d\vec{\beta}/dt + (d\vec{\beta}/dt \cdot \hat{n})(\vec{\beta} - \hat{n})], \quad (\text{A5})$$

where \hat{n} is the direction toward the observer, so $(1 - \vec{\beta} \cdot \hat{n})$ is the familiar factor, $(1 - \beta \cos \theta)$. In the analysis that follows, we take $\vec{\beta} = \beta \hat{\beta}$ to be a vector in a spherical-polar coordinate system with the z -axis oriented towards the observer, such that $\hat{n} = \hat{z} = \cos \theta \hat{\beta} - \sin \theta \hat{\theta}$, see Figure A1. The unit vector, $\hat{\theta}$, defines the direction of increasing angle to the line of sight, and the angle ϕ is the polar angle in the plane of the sky. In these coordinates, $d\vec{\beta}/dt = \dot{\beta} \hat{\beta} + \beta \dot{\theta} \sin \theta \hat{\phi} + \beta \dot{\theta} \hat{\theta}$, where we note that $\hat{\phi}$ is perpendicular to both $\hat{\beta}$ and $\hat{\theta}$ and is therefore always perpendicular to the observed motion in the plane of the sky.

To find the observed parallel acceleration, along the direction of observed motion in the plane of the sky, we take the dot product of Equation (A5) with the unit vector along $\vec{\beta}_{\text{obs}}$, $\hat{\beta}_{\text{obs}} = \sin \theta \hat{\beta} + \cos \theta \hat{\theta}$.

$$\frac{d\beta_{\parallel \text{obs}}}{dt_{\text{obs}}} = \frac{d\vec{\beta}_{\text{obs}}}{dt_{\text{obs}}} \cdot \hat{\beta}_{\text{obs}} = \frac{\dot{\beta} \sin \theta + \beta \dot{\theta} (\cos \theta - \beta)}{(1 - \beta \cos \theta)^3}. \quad (\text{A6})$$

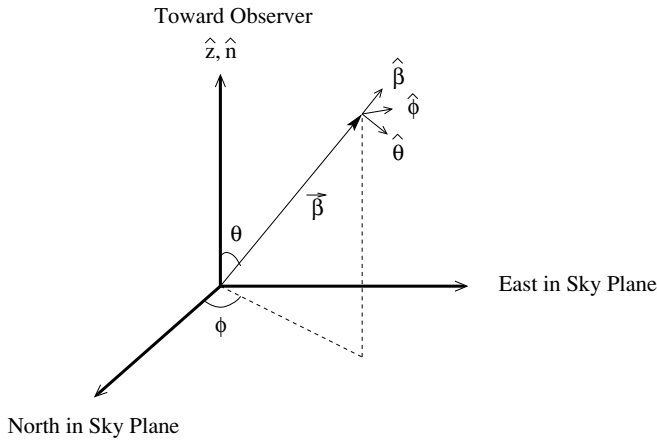


Figure A1. Three-dimensional geometry of the velocity vector, $\vec{\beta}$, which is taken in the text to be a vector in a standard spherical-polar coordinate system, as illustrated. The unit vectors $\hat{\beta}$, $\hat{\phi}$, $\hat{\theta}$ are mutually orthogonal.

As expected, this expression matches what we would get by simply differentiating the familiar apparent speed expression given in Equation (1) and correcting for the appropriate time frames as described in the previous section.

To find the observed perpendicular acceleration, transverse to the direction of observed motion in the plane of the sky, we simply take the dot product of Equation (A5) with $\hat{\phi}$:

$$\frac{d\beta_{\perp\text{obs}}}{dt_{\text{obs}}} = \frac{d\vec{\beta}_{\text{obs}}}{dt_{\text{obs}}} \cdot \hat{\phi} = \frac{\beta \dot{\phi} \sin \theta}{(1 - \beta \cos \theta)^2}, \quad (\text{A7})$$

so the observed perpendicular acceleration is only related to changes in the angle ϕ , as we might expect.

REFERENCES

Bach, U., Kadler, M., Krichbaum, T. P., Middelberg, E., Alef, W., Witzel, A., & Zensus, J. A. 2005, in ASP Conf. Ser. 340, *Future Directions in High Resolution Astronomy*, ed. J. Romney & M. Reid (San Francisco, CA: ASP), 30
 Blandford, R. D., & Königl, A. 1979, *ApJ*, **232**, 34

Britzen, S., et al. 2008, *A&A*, **484**, 119
 Cara, M., & Lister, M. L. 2008, *ApJ*, **674**, 111
 Cooper, N. J., Lister, M. L., & Kochanzyk, M. D. 2007, *ApJS*, **171**, 376
 Gómez, J.-L., Marscher, A. P., Alberdi, A., Jorstad, S. G., & Agudo, I. 2001, *ApJ*, **561**, L161
 Hardcastle, M. J., Alexander, P., Pooley, G. G., & Riley, J. M. 1999, *MNRAS*, **304**, 135
 Homan, D. C., & Lister, M. L. 2006, *AJ*, **131**, 1262
 Homan, D. C., Lister, M. L., Kellermann, K. I., Cohen, M. H., Ros, E., Zensus, J. A., Kadler, M., & Vermeulen, R. C. 2003, *ApJ*, **589**, L9
 Homan, D. C., Ojha, R., Wardle, J. F. C., Roberts, D. H., Aller, M. F., Aller, H. D., & Hughes, P. A. 2001, *ApJ*, **549**, 840
 Jorstad, S. G., Marscher, A. P., Lister, M. L., Stirling, A. M., Cawthorne, T. V., Gómez, J.-L., & Gear, W. K. 2004, *AJ*, **127**, 3115
 Jorstad, S. G., et al. 2005, *AJ*, **130**, 1418
 Kellermann, K. I., Vermeulen, R. C., Zensus, J. A., & Cohen, M. H. 1998, *AJ*, **115**, 1295
 Kellermann, et al. 2004, *ApJ*, **609**, 539
 Kovalev, Y. Y., et al. 2005, *AJ*, **130**, 2473
 Kovalev, Y. Y., et al. 2009, *ApJ*, **696**, L17
 Lister, M. L. 2006, *BAAS*, **38**, 905
 Lister, M. L., & Homan, D. C. 2005, *AJ*, **130**, 1389
 Lister, M. L., Homan, D. C., Kadler, M., Kellermann, K. I., Kovalev, Y. Y., Ros, E., Savolainen, T., & Zensus, J. A. 2009a, *ApJ*, **696**, L22
 Lister, M. L., & Marscher, A. P. 1997, *ApJ*, **476**, 572
 Lister, M. L., et al. 2009b, *AJ*, **137**, 3718
 Lister, M. L., et al. 2009c, *AJ*, in press (arXiv:0909.5100)
 Marscher, A. P., & Gear, W. K. 1985, *ApJ*, **298**, 114
 Meier, D. L., Koide, S., & Uchida, Y. 2001, *Science*, **291**, 84
 Mullin, L. M., & Hardcastle, M. J. 2009, *MNRAS*, **398**, 1989
 Piner, B. G., Bhattarai, D., Edwards, P. G., & Jones, D. L. 2006, *ApJ*, **640**, 196
 Piner, B. G., Mahmud, M., Fey, A. L., & Gospodinova, K. 2007, *AJ*, **133**, 2357
 Sambruna, R. M., Gambill, J. K., Maraschi, L., Tavecchio, F., Cerutti, R., Cheung, C. C., Urry, C. M., & Chartas, G. 2004, *ApJ*, **608**, 698
 Savolainen, T., Wiik, K., Valtaoja, E., & Tornikoski, M. 2006, *A&A*, **446**, 71
 Sikora, M., Begelman, M. C., Madejski, G. M., & Lasota, J.-P. 2005, *ApJ*, **625**, 72
 Stirling, A. M., et al. 2003, *MNRAS*, **341**, 405
 Vlahakis, N., & Königl, A. 2004, *ApJ*, **605**, 656
 Wardle, J. F. C., & Aaron, S. E. 1997, *MNRAS*, **286**, 425
 Wardle, J. F. C., Cawthorne, T. V., Roberts, D. H., & Brown, L. F. 1994, *ApJ*, **437**, 122
 Wehrle, A. E., Piner, B. G., Unwin, S. C., Zook, A. C., Xu, W., Marscher, A. P., Teräsranta, H., & Valtaoja, E. 2001, *ApJS*, **133**, 297
 Zavala, R. T., & Taylor, G. B. 2001, *ApJ*, **550**, L147
 Zensus, A., Ros, E., Kellermann, K. I., Cohen, M. H., & Vermeulen, R. C. 2002, *AJ*, **124**, 662
 Zensus, J. A., Cohen, M. H., & Unwin, S. C. 1995, *ApJ*, **443**, 35

ERRATUM: “MOJAVE: MONITORING OF JETS IN ACTIVE GALACTIC NUCLEI WITH VLBA EXPERIMENTS. VII. BLAZAR JET ACCELERATION” (2009, *ApJ*, 706, 1253)

D. C. HOMAN¹, M. KADLER^{2,3,4,5}, K. I. KELLERMANN⁶, Y. Y. KOVALEV^{7,8},
 M. L. LISTER⁹, E. ROS^{7,10}, T. SAVOLAINEN⁷, AND A. ZENSUS⁷

¹ Department of Physics and Astronomy, Denison University, Granville, OH 43023, USA; homand@denison.edu

² Dr. Remeis-Sternwarte Bamberg, Universität Erlangen-Nürnberg, Sternwartstrasse 7, D-96049 Bamberg, Germany; matthias.kadler@sternwarte.uni-erlangen.de

³ Erlangen Centre for Astroparticle Physics, Erwin-Rommel Str. 1, D-91058 Erlangen, Germany

⁴ CRESST/NASA Goddard Space Flight Center, Greenbelt, MD 20771, USA

⁵ Universities Space Research Association, 10211 Wincopin Circle, Suite 500, Columbia, MD 21044, USA

⁶ National Radio Astronomy Observatory, 520 Edgemont Road, Charlottesville, VA 22903-2475, USA; kkellerm@nrao.edu

⁷ Max-Planck-Institut für Radioastronomie, Auf dem Hügel 69, D-53121 Bonn, Germany; Eduardo.Ros@uv.es, tsavolainen@mpifr-bonn.mpg.de, zensus@mpifr-bonn.mpg.de

⁸ Astro Space Center of Lebedev Physical Institute, Profsoyuznaya 84/32, 117997 Moscow, Russia; yyk@asc.rssi.ru

⁹ Department of Physics, Purdue University, 525 Northwestern Avenue, West Lafayette, IN 47907, USA; mlister@purdue.edu

¹⁰ Departament d’Astronomia i Astrofísica, Universitat de València, E-46100 Burjassot, València, Spain

Received 2014 October 14; published 2014 November 14

Figure 10, which examines a correlation between perpendicular acceleration and non-radial motion, had two data points that were

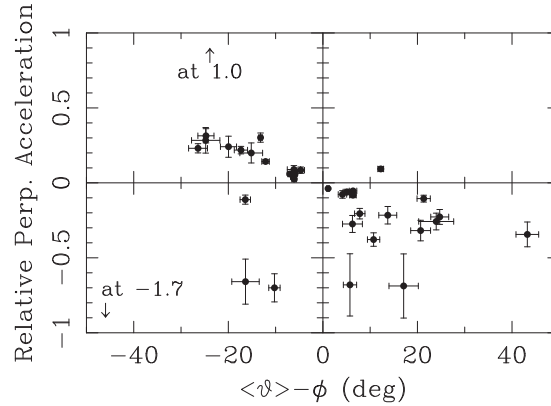


Figure 10. Corrected version the figure showing relative perpendicular acceleration vs. $\langle\vartheta\rangle - \phi$ for all jet components with both significant non-radial motion and perpendicular acceleration. The correction moved two data points from the lower left quadrant to the lower right.

plotted in the wrong quadrant due to an error in sign conversion for position angles very near $\pm 180^\circ$. No other results in the paper were affected. Correcting this error strengthens the statistical relationship shown in the plot from 30 out of 37 to 32 out of 37 non-radial motions in the correct direction to have been caused by the observed acceleration. A corrected version of the figure appears below. An updated version of this relationship is examined in the MOJAVE series paper, MOJAVE XII (Homan et al. 2014).

REFERENCE

Homan, D. C., Kadler, M., Kellermann, K. I., et al. 2014, *ApJ*, in press (arXiv:1410.8502)

ERRATUM: “MOJAVE: MONITORING OF JETS IN ACTIVE GALACTIC NUCLEI WITH VLBA EXPERIMENTS. VII. BLAZAR JET ACCELERATION” (2009, *ApJ*, 706, 1253)

D. C. HOMAN¹, M. KADLER^{2,3,4,5}, K. I. KELLERMANN⁶, Y. Y. KOVALEV^{7,8},
 M. L. LISTER⁹, E. ROS^{7,10}, T. SAVOLAINEN⁷, AND A. ZENSUS⁷

¹ Department of Physics and Astronomy, Denison University, Granville, OH 43023, USA; homand@denison.edu

² Dr. Remeis-Sternwarte Bamberg, Universität Erlangen-Nürnberg, Sternwartstrasse 7, D-96049 Bamberg, Germany; matthias.kadler@sternwarte.uni-erlangen.de

³ Erlangen Centre for Astroparticle Physics, Erwin-Rommel Str. 1, D-91058 Erlangen, Germany

⁴ CRESST/NASA Goddard Space Flight Center, Greenbelt, MD 20771, USA

⁵ Universities Space Research Association, 10211 Wincopin Circle, Suite 500, Columbia, MD 21044, USA

⁶ National Radio Astronomy Observatory, 520 Edgemont Road, Charlottesville, VA 22903-2475, USA; kkellerm@nrao.edu

⁷ Max-Planck-Institut für Radioastronomie, Auf dem Hügel 69, D-53121 Bonn, Germany;

Eduardo.Ros@uv.es, tsavolainen@mpifr-bonn.mpg.de, zensus@mpifr-bonn.mpg.de

⁸ Astro Space Center of Lebedev Physical Institute, Profsoyuznaya 84/32, 117997 Moscow, Russia; yyk@asc.rssi.ru

⁹ Department of Physics, Purdue University, 525 Northwestern Avenue, West Lafayette, IN 47907, USA; mlister@purdue.edu

¹⁰ Departament d’Astronomia i Astrofísica, Universitat de València, E-46100 Burjassot, València, Spain

Received 2014 October 14; published 2014 November 14

Figure 10, which examines a correlation between perpendicular acceleration and non-radial motion, had two data points that were plotted in the wrong quadrant due to an error in sign conversion for position angles very near $\pm 180^\circ$. No other results in the paper were affected. Correcting this error strengthens the statistical relationship shown in the plot from 30 out of 37 to 32 out of 37 non-radial motions in the correct direction to have been caused by the observed acceleration. A corrected version of the figure appears below. An updated version of this relationship is examined in the MOJAVE series paper, MOJAVE XII (Homan et al. 2014).

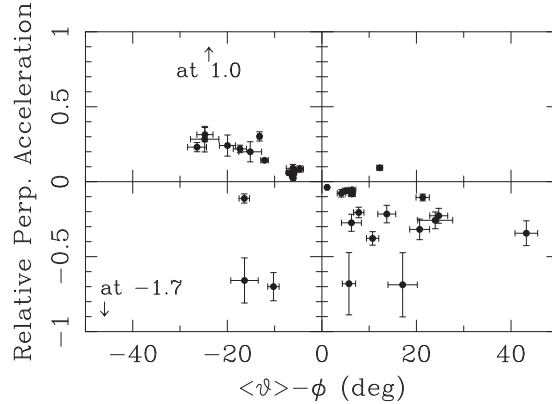


Figure 10. Corrected version the figure showing relative perpendicular acceleration vs. $\langle\psi\rangle-\phi$ for all jet components with both significant non-radial motion and perpendicular acceleration. The correction moved two data points from the lower left quadrant to the lower right.

REFERENCE

Homan, D. C., Kadler, M., Kellermann, K. I., et al. 2014, *ApJ*, in press (arXiv:1410.8502)